# Tracer Diffusion at Water-Oil Interfaces studied by Fluorescence Correlation Spectroscopy

## Dissertation

zur Erlangung des Grades

"Doktor der Naturwissenschaften"

am Fachbereich Chemie

der Johannes Gutenberg-Universität in Mainz

Dapeng Wang

geb. am 03.01.1984

in Qingdao (China)

Mainz-2012

1. Berichterstatter: Prof. Dr. Hans-Jürgen Butt

2. Berichterstatter: Prof. Dr. Carsten Sönnichsen

Tag der mündlichen Prüfung:

# Contents

# ABSTRACT

The adsorption of particles and surfactants at water-oil interfaces has attracted continuous attention because of its emulsion stabilizing effect and the possibility to form two-dimensional materials. Herein, I studied the interfacial diffusion of single molecules and nanoparticles at water-oil interfaces using fluorescence correlation spectroscopy.

Fluorescence correlation spectroscopy (FCS) is a promising technique to study diffusion of fluorescent tracers in diverse conditions. This technique monitors and analyzes the fluorescence fluctuation caused by single fluorescent tracers coming in and out of a diffraction-limited observation volume "one at a time". Thus, this technique allows a combination of high precision, high spatial resolution and low tracer concentration.

In chapter 1, I discussed some controversial questions regarding the properties of water-hydrophobic interfaces and also introduced the current progress on the stability and dynamic of single nanoparticles at water-oil interfaces. The materials and setups I used in this thesis were summarized in chapter 2.

In chapter 3, I presented a new strategy to study the properties of water-oil interfaces. The two-dimensional diffusion of isolated molecular tracers at water/n-alkane interfaces was measured using fluorescence correlation spectroscopy. The diffusion coefficients of larger tracers with a hydrodynamic radius of 4.0 nm agreed well with the values calculated from the macroscopic viscosities of the two bulk phases. However, for small molecule tracers with

hydrodynamic radii of only 1.0 and 0.6 nm, notable deviations were observed, indicating the existence of an interfacial region with a reduced effective viscosity.

In chapter 4, the interfacial diffusion of nanoparticles at water-oil interfaces was investigated using FCS. In stark contrast to the interfacial diffusion of molecular tracers, that of nanoparticles at any conditions is slower than the values calculated in accordance to the surrounding viscosity. The diffusion of nanoparticles at water-oil interfaces depended on the interfacial tension of liquid-liquid interfaces, the surface properties of nanoparticles, the particle sizes and the viscosities of surrounding liquid phases. In addition, the interfacial diffusion of nanoparticles with Janus motif is even slower than that of their symmetric counterparts. Based on the experimental results I obtained, I drew some possibilities to describe the origin of nanoparticle slowdown at water-oil interfaces.

# CHAPTER 1

## Introduction and motivation

### 1.1 Water-oil interfaces

Water is the most common liquid on earth and constitutes a major part of living organisms. Not surprisingly therefore its structure, properties, and interactions with other substances have been continuously studied from ancient times to nowadays. One particularly interesting question is what exactly happens when water meets hydrophobic molecules or surfaces [1, 2]. The term hydrophobic is commonly used to describe nonpolar molecules e.g. n-alkanes (or oils in general) that, when mixed with water, separate into a water-rich and an oil-rich phases. The reason for separation is the fact that nonpolar molecules are not able to form hydrogen bonds with the polar water molecules. As a result, water repels them in favor of bonding with itself to form a randomly fluctuating network [1, 3]. Proximity of water to an extended hydrophobic surface, however, disrupts the hydrogen-bonding pattern, and thus changes the water properties near the interface [4-6]. Despite the fact that the concept of the hydrophobic effect is well understood, only recently the theoretical and experimental exploration begun to interpret how water meets hydrophobic molecules in a microscopic view.

In this chapter, the basic properties of bulk water and the concept of the interfacial tension and contact angle are introduced. Afterwards, the controversial question about the properties of water molecules in proximity to a hydrophobic surface is reviewed.

### 1.1.1 Properties of bulk water

Water ($H_2O$) is a chemical substance. A water molecule possesses two hydrogen atoms covalently bonded to an oxygen atom with the H-O-H bond angle of 104.45º. In principle, each water molecule can form four hydrogen bonds with neighboring water molecules in an arranged tetrahedral structure in bulk water, as shown in Fig.1.1. The binding energy of a hydrogen bond in water is roughly 12 kJ mol$^{-1}$. Thus, this leads to strong hydrogen bond networks in bulk water, which cause a number of unique properties of water, including a high surface tension (72.8 mN m$^{-1}$), a large evaporation heat (40.7 kJ mol$^{-1}$), a high viscosity (1 cP) and an enhanced boiling point (273.15 K) compared to compounds with a similar structure, e.g., sulfureted hydrogen, hydrogen chloride, etc.
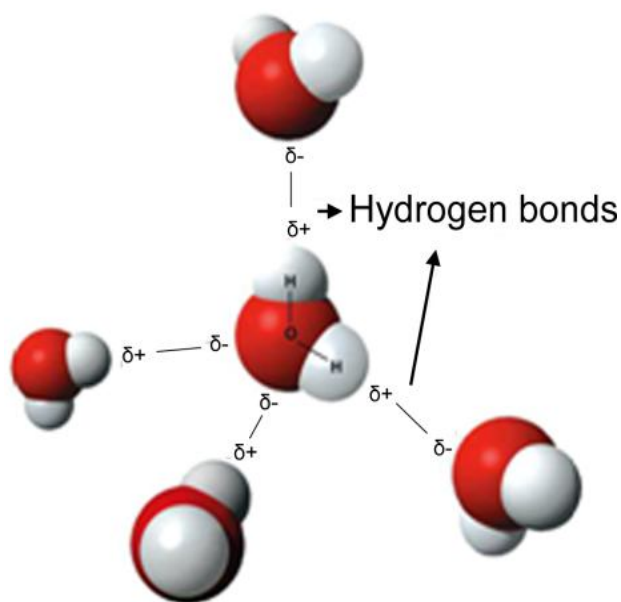


***Figure 1.1*** *A model of the hydrogen bond network in bulk water. This picture is obtained from http://en.wikipedia.org/wiki/Water.*

The structural information of water in bulk can be obtained by X-ray [7, 8] and neutron reflectivity measurements [9]. The average distance of neighboring water molecules was estimated to be approximately 2.8 Å from the oxygen-oxygen correlation function $g_{OO}(r)$ and the Fourier transform of the partial liquid structure factor $S_{OO}(q)$. The correlation length of bulk water is 4 -8 Å, as estimated by small-angle X-ray and neutron scattering measurements [10, 11]. This is roughly equal to two times the water diameter.

A phase diagram shows the macroscopic physical states in that chemical substances could be in response to pressure and temperature. Water is in the liquid state at room temperature and standard atmospheric pressure. It becomes solid, i.e., ice, if the temperature is lowered than 273.15 K or gaseous, i.e., water vapor, if the temperature is above 373 K. Each line (phase line) on a phase diagram represents a phase boundary and gives the conditions in which two phases may stably coexist, as demonstrated in Fig.1.2.



***Figure 1.2*** *Phase diagram of water. This picture has not been scaled. The phase diagram of water consists of fifteen phases of crystalline ice and several solid amorphous phases[12].*

*These phases are not shown here for simplicity.*

In vicinity to a phase boundary, a slight change in pressure or temperature may result in an abruptly transition from one physical state to another. Where thr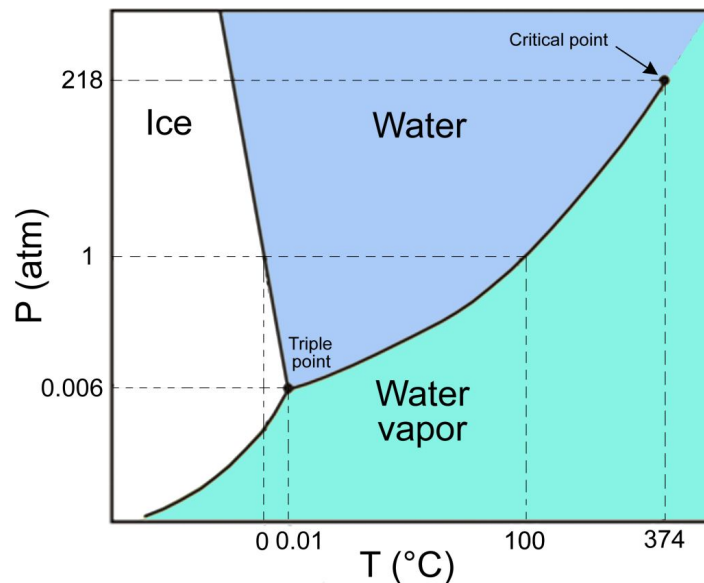ee phase lines meet, there is a so-called "triple point", where the boiling point of water and melting point of ice are akin. In the "triple point", liquid water, gaseous water and solid stably coexist. A "critical point" often exists at the end of a phase line because the properties of the two phases become indistinguishable from each other. The critical point is usually found at the high pressure end of the liquid-gas phase line, as shown in Fig.1.2.

## 1.1.2 Interfacial tension and contact angle

Interfacial tension is a parameter that quantifies the ability of an interface to resist an external force. Interfacial tension has dimensions of force per unit area. The term "interfacial tension" would suggest that the interface stays under a tension. The situation is similar to a rubber balloon, in which a force is needed to increase the surface area against an applied tension. However, there is a difference between the liquid interface and the rubber balloon: the stretching of a rubber film is usually elastic while the expansion of a liquid surface is a plastic process [13].

The origin of the interfacial tension can be understood on a molecular level. Here water interfaces are used as an example. For water molecules it is energetically favorable to be surrounded by other water molecules in order to maintain the hydrogen bond networks. Without these networks, water would not be a condensed phase at all at ambient conditions, but it would exist only in vapor phase. At the interface adjacent to an immiscible phase, water molecules are only partially surrounded by other water molecules and the number of adjacent

molecules is smaller than in the bulk. In particular, in order to bring a water molecule from the bulk to an interface, work has to be done to break apart hydrogen bonds. This is energetically unfavorable. Therefore, the interfacial tension γ can be explained as the energy required to bring a molecule from the bulk to the interface.
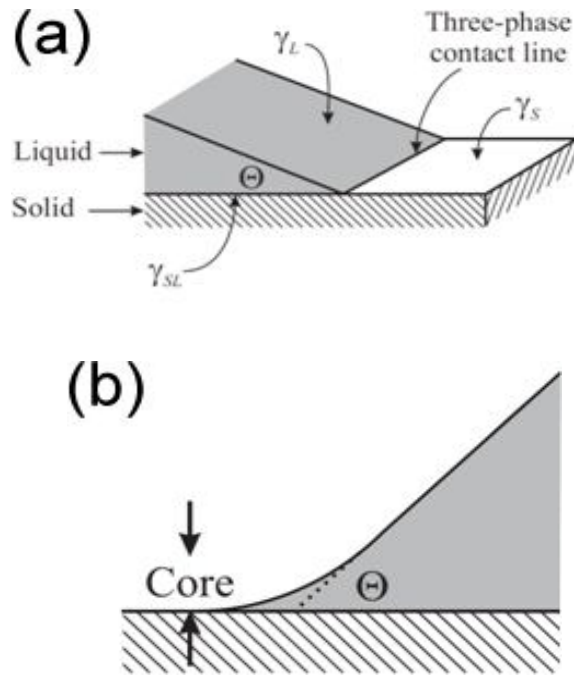


*Fig.1.3 (a) A scheme of a liquid droplet with a contact angle Θ on the top of a solid surface.*

*(b) A microscopic view of contact region for a repulsive force between the solid-liquid and liquid-gas interface. This picture is reprinted from Ref. [13].*

When a liquid droplet sits on a solid surface, at the boundary three phases meet (Fig.1.3). The contact angle can be described according to the interfacial tensions of (solid-gas, $\gamma_{SV}$, solid-liquid, $\gamma_{SL}$, and liquid-gas interfaces, $\gamma_{LV}$) as follows,

$$\cos\theta = \frac{\gamma_{SV} - \gamma_{SL}}{\gamma_{LV}} \qquad (1.1)$$

The Eq.1.1 is Young's equation. If $\gamma_{SV}$ is higher than $\gamma_{SL}$, $\cos\theta$ is positive and the contact angle is smaller than 90º; the liquid can wet the solid. If $\gamma_{SV} < \gamma_{SL}$, $\cos\theta$ is negative and the contact angle exceeds 90º.

The contact angle $\theta$ at a microscopic scale (0.1µm or less) may deviate from what one calculated by Young's equation due to surface forces, e.g., long-range van der Waals and double-layer forces, etc [14]. To establish a new wetting line, energy is required. This energy per unit length is referred to as the line tension $\kappa$. The line tension should be taken into account at a small length scale, by introducing an additional term into Young's equation [15]:

$$\cos\theta = \frac{\gamma_{SV} - \gamma_{SL} - \dfrac{\kappa}{a}}{\gamma_{LV}} \qquad\qquad (1.2)$$

Here, $\alpha$ is the curvature radius of the three phase line. The line tension can be either positive or negative. Typical values of line tension are in the order of $10^{-10}$-$10^{-11}$N [16, 17].

## 1.1.3 Theoretical description of water-hydrophobic interfaces

The interfacial structure of water-hydrophobic interfaces has aroused special interest of scientists over twenty years. But one may be surprised to learn that the question how water molecules behave at interfaces has caused serious controversy in various experimental studies. Theoretical considerations suggested the presence of a reduced water density region adjacent to hydrophobic moieties [1, 18, 19]. Indeed, on solid hydrophobic surfaces this so-called "hydrophobic gap" has been predicted by computer simulations [20-22].

Below, a seemingly well-known microscopic calculation is introduced, which confirmed the existence of a reduced water density region in proximity to a hydrophobic

surface/molecule. But it should be mentioned that there are several studies which present an opposite physical picture [23, 24]. In fact, it is rather difficult to rationalize the interfacial structure at an angstrom scale in real world.
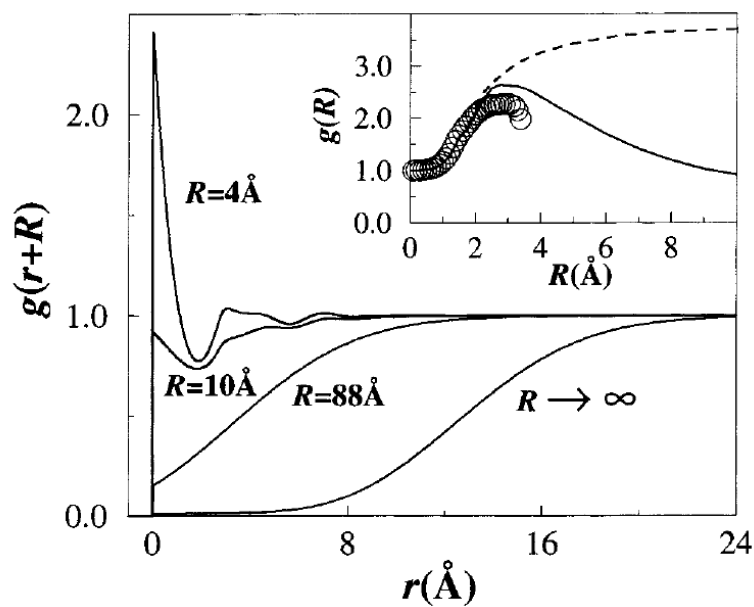


***Figure 1.4*** *Average equilibrium density of water g(r+R) at a distance r + R from the center of hydrophobic molecule as a function of distance r. This picture is reprinted from Ref.*[19].

As hydrophobic molecules are not able to form hydrogen bonds with water molecules, the resulting energetic effect could lead to a drying effect [18]. However, the van der Waals interactions ensure that no macroscopic separation can be observed at a macroscopic scale. The behavior of water near a hydrophobic molecule can be described based on the average equilibrium density of water $g(r+R)$ at a distance $r$ towards the center of a hydrophobic molecule with radius $R$ (Fig.1.4). The calculation procedure can be found in Ref.[18, 19, 25, 26]. If $R$ is small, the hydrogen bond networks in proximity of a hydrophobic molecule could be maintained but with a small distortion. Thus, the water density close to a hydrophobic

molecule is increased due to the elastic response to the distortion [1, 2]. As the size of the hydrophobic molecules increases, the source of elasticity, i.e., the hydrogen bonding network is eliminated. As illustrated in Fig.1.4, the density of water close to an unlimited planar hydrophobic surface is rather low over more than eight angstroms.

## 1.1.4 Experimental studies of water-hydrophobic interfaces

With respect to water-hydrophobic interfaces, in 1994 Du and coworkers found that the sum frequency generation spectra in the OH-bonding region at a water/n-hexane interface exhibited a large similarity with the signal from a water/vapor surface while those recorded on a hydrophobic solid substrate showed a remarkable difference[4]. Today this difference is commonly attributed to a different arrangement of water molecules near a thermally fluctuating fluid interface as compared to a rigid hard wall [27]. A different arrangement might also be the reason why experimental studies [28, 29] have never detected a pronounced depletion layer at liquid-liquid interfaces.

In this part, I summarized the current experimental progress of how water molecules meet a hydrophobic surface at an angstrom scale, using several optical methods, such as ellipsometry, neutron and X-ray reflectivity.

*Ellipsometry*

Ellipsometry is an optical technique that can be used to measure various properties of thin films with information obtained by detecting the incident angle and polarization dependence of reflected light.  As an optical technique, spectroscopic ellipsometry is

contactless and non-destructive. For layers much smaller than the optical wavelength, the layer thickness can be reflected by measuring the change of the refractive index. Even though Castro et al. [30] firstly reported a vapor-like layer with thickness of 5-10 Å, other studies [31-33] found no indication of a depleted density layer at solid hydrophobic-water interfaces by ellipsometry with an experimental resolution of 1 Å.


*Neutron reflectivity*

Neutron reflectivity is a neutron diffraction technique for measuring the structure of thin films with high sensitivity by means of the interfacial scattering profile at interfaces. Although specific technical details are not provided here, it is worth to mention that the neutron reflectivity has several advantages over other techniques, e.g., over X-ray or ellipsometry. First, the scattering contrast can be tailored by isotope ratios. In addition, the neutron reflectivity is considered as the best tool to probe the density profile because the absorption of neutrons is quite small in various materials. But such advantages are overcompensated by its disadvantages, including a low neutron flux and a high background signal. Thus, the information obtained at water-hydrophobic interfaces by neutron reflectivity measurements was also under debate. Different groups reported different values for the thickness of the depleted density layer, ranging from 0 Å [34], to 5Å (degassed water) [35, 36], up to unphysical values, 2-5nm [37, 38].

The effect of dissolved gasses on the interfacial properties was another debated issue. To the best of my knowledge, all previous studies involving dissolved gasses were done for water-hydrophobic solid interfaces. A neutron reflectivity measurement showed that the

depletion layer for water saturated with Ar is 2 or 3 times smaller than that for degassed water [35]. But other studies indicated an opposite physical picture [39, 40]. In addition, it should be mentioned that two X-ray reflectivity studies exhibited no gas-relevant effect at water-hydrophobic surfaces [41, 42].

*X-ray reflectivity*

X-ray reflectivity could monitor the depth profile of the electron density. In general, a X-ray beam is reflected from a flat surface and the reflected X-rays intensity in the specular direction could be detected. The X-ray scattering can be analyzed to obtain the density profile normal to the surface based on the Fresnel's law of reflectivity.

The overall picture emerging from these studies is consistent with an interfacial depletion length corresponding to less than a monolayer of water at solid hydrophobic-water interfaces [41-43]. Typical curves are shown in Fig.1.5a. The origin of the observed molecular scale depletion includes contributions from the reduced density of terminal methyl groups[44], generic packing effects of liquids adjacent to a solid wall [45], the complex interplay between the water structure and the topography of the hydrophobic surface [20, 46].
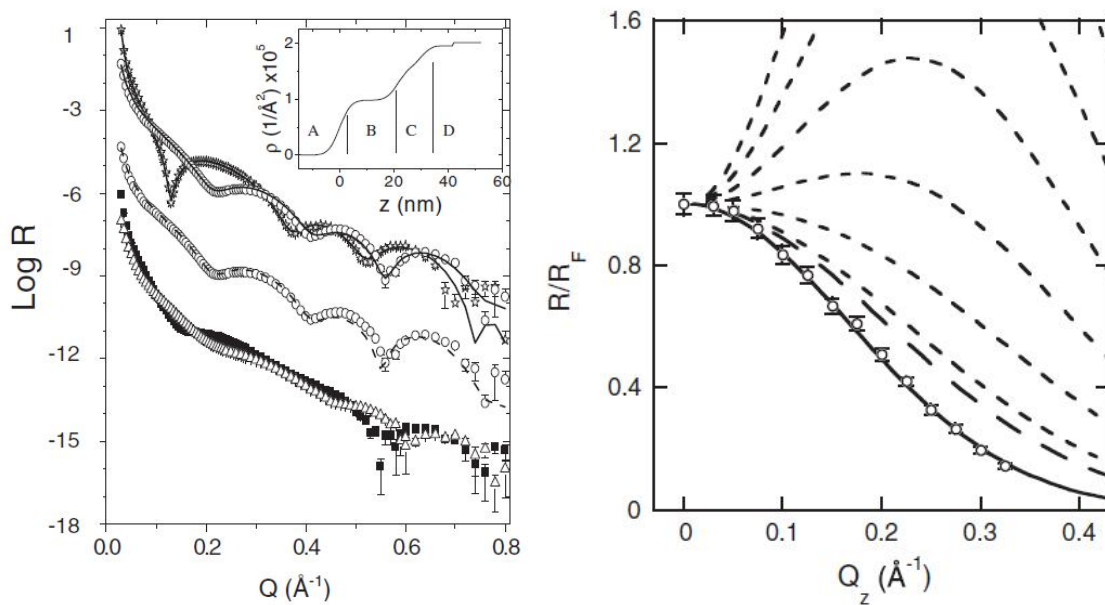
***Figure 1.5*** *(left) X-ray reflectivity plots for a hydrophobic solid surface monolayer in air (open stars) and water (open circles) and for a low-quality hydrophobic solid surface exposed to air (solid squares) and ambient water (open triangles). Solid lines through the data show the best fits. This picture is reprinted from Ref.[42]. (right) X-ray reflectivity plots for a heptane-water interface. The dashed lines indicate different fits in which different sizes of depletion layer are assumed. The solid lines indicate the fit with no depleted density layer. This picture is reprinted from Ref.[29].*

However, it should be mentioned that the depleted density layer at water-solid hydrophobic interfaces may depend on the surface roughness [46] and could in turn be sample-dependent [46-48]. In addition, in different X-ray reflectivity studies, no depleted density region was identified at liquid-liquid interfaces, as shown in Fig. 1.5b.

## 1.2 Nanoparticles at water-oil interfaces

The absorption of small particles at a liquid-liquid interface has attracted continuous attention ever since its emulsion stabilizing effect was discovered over a century ago [49]. Nowadays it is obvious that a good understanding of the dynamics and self-organization of nanometer-sized objects, e.g., molecules, macromolecules and nanoparticles (NPs) at immiscible liquid-liquid interfaces is of fundamental interest for soft mater physics and cell biology. It is also important for a number of technological applications in material synthesis, pharmacy, microfluidics and nanotechnology. For example, it is essential for the fabrication of new materials based on two or three-dimensional ordered NPs with unique optical, magnetic and electronic properties [50-53] or for the emulsion effects [54-56].

The use of WO interfaces as templates to self-assemble the colloidal particles into 2D ordering structures, which exhibit tunable optical, electrical magnetic properties, has attracted considerable attention. A number of studies have reported various 2D nanoparticle films that could be formed at WO interfaces for diverse applications. To organize the particles into an ordered structure, a modest dynamic freedom is prerequisite and once completed, the established structure is necessary to be stabilized. Thus, how single nanoparticles behave at water-oil interfaces is very important in the formation of the 2D materials.

Since the study of single nanoparticles at interfaces is still on the early stage, in this section, the theoretical description for the stability of nanoparticles at WO interfaces is reviewed. Furthermore some theoretical models describing the diffusion of particles at liquid interfaces are introduced. Finally, I consider a recent experimental study in which the diffusion of polystyrene colloids at a heptane-water interface was investigated by evanescent-wave dynamic light scattering.

## 1.2.1 Stability of symmetric particles at water-oil interfaces

The phenomenon that particles enrich at WO interfaces to form a resistant particle-film was firstly discovered over a century ago. The particles spontaneously self-assemble into a resistant particle film at immiscible liquid-liquid interfaces to inhibit the coalescence of emulsion drops. These Pickering emulsions are spontaneously formed, because the free energy of the whole systems could be favorably decreased. The theoretical model of the absorption behavior was given by Pieranski [57], who suggested that the interfacial energy between water and oil could be reduced by placing a particle at the interfaces, yielding an energy difference $\Delta E$ as follows:

$$\Delta E = -\frac{\pi \bullet r^2}{\gamma_{WO}}[\gamma_{WO} - (\gamma_{SW} - \gamma_{SO})]^2 \qquad (1.3)$$

Here, $r$ is the particle radius, $\gamma_{WO}$, $\gamma_{SW}$, $\gamma_{SO}$, are the interfacial tension of water-oil, particle-water and particle-oil interfaces, respectively. Eq. 1.3 exhibits that in a given system, when a particle is placed at an interface, the total free energy drop is proportional to the square of the particle size $r$. For a μm-sized particle, the decrease in free energy is much higher than the thermal energy (several $k_BT$). This results in an effective adhesion of particles at interfaces. When the particle size is decreased down to a nanometer scale, the reduced free energy becomes comparable to the thermal energy. As a result, the nanoparticles could be frequently de-attached from (re-attached to) the interfaces, and as such, the absorption-desorption is in equilibrium.
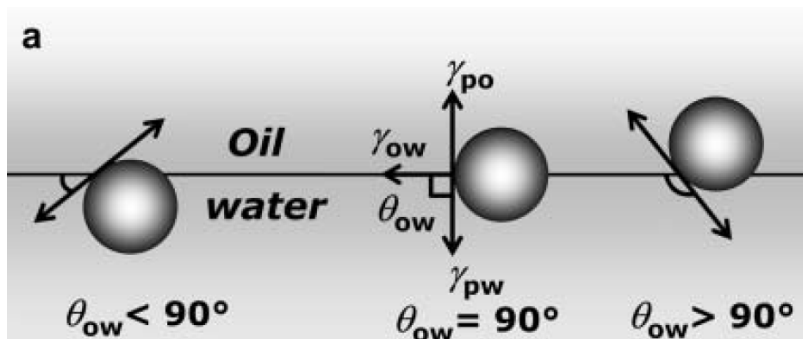
*Figure 1.6* *A scheme of placing a particle at water-oil interfaces with a contact angle less than 90º (left), equal to 90º (middle), and larger than 90º (right). This picture is reprinted from Ref.[51].*

When a particle is placed at an interface, it should be mentioned that the contact angle could be described by the Young equation. Fig. 1.6 shows three different cases when a particle is placed at a WO interface. Then the decrease in free energy according to the contact angle can be given as [58]

$$\Delta E = -\pi \bullet r^2 \gamma_{wo}[1 \pm \cos\theta]^2 \tag{1.4}$$

The total free energy change for placing a silica particle ($R$ = 10nm) with diverse contact angle at a planar water-toluene interface was first calculated by Binks et al, as shown in Fig. 1.7. For simplicity, they neglected the effect of line tension. A maximum at a contact angle of 90º with roughly $2800 k_B T$ was achieved for a nanoparticle ($R$= 10nm). The desorption energy was decreased notably as decreasing the particle size. Alternatively, Lin et al. have estimated the desorption energy by Eq.1.3, yielding a value of roughly 5 $k_B T$ for CdSe nanoparticles ($R$= 1.4nm) attached at a water-toluene interface [50]. The small desorption energy resulted in escape-capture equilibrium for nanoparticles at interfaces. These

22

values which were inferred from the thermodynamic model were consistent with the experimental observation.
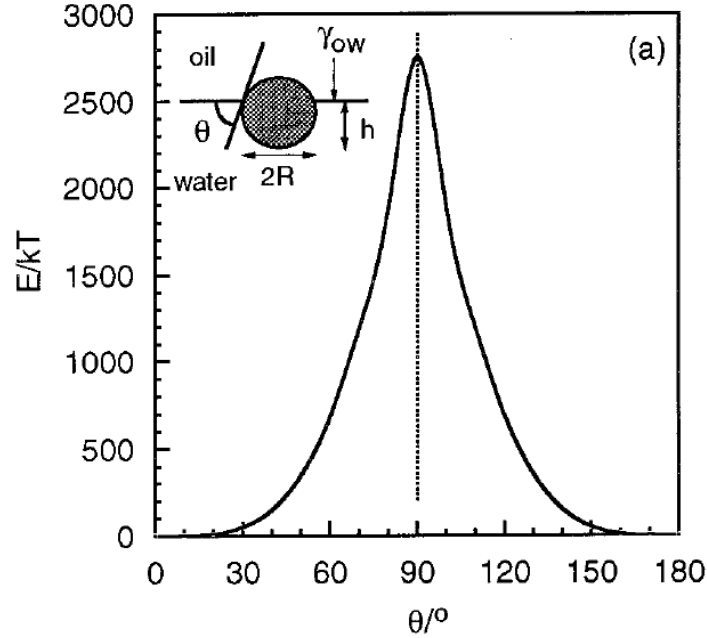


*Figure 1.7* *Desorption energy of a silica spherical particle (R= 10nm) at a water-toluene interface as a function of the contact angle. This picture is reprinted from Ref.* [58].

However, the contact angle for a particle at a WO interface might deviate from what Young's equation expects because of the line tension $\kappa$, which becomes increasingly important as the particle radius $r$ is decreased. In a different approach, Aveyard and Clent deduced an expression regarding the variation of free energy integrating the effect of line tension as follows [59]:

$$\bar{F} = -\pi r^2 \gamma_{WO}(1-\bar{z}^2) + 2\pi r^2(\gamma_{SW}-\gamma_{SO})(1-\bar{z}) + 2\pi r \kappa \sqrt{1-\bar{z}^2} \tag{1.5}$$

23

Here, $R$ is the particle radius, $\bar{z}$ is defined as $\bar{z} = z/R$ in which $z = 0$ corresponds to the middle of the interface (where the center of the particles is placed). Based on the theoretical calculation, the line tension $\kappa$ was expected to be on the order of magnitude of $10^{-10}$-$10^{-11}$N, either positive or negative, as described above. Aveyard et al. used a different strategy to measure the line tension by monitoring the surface pressure. They found the line tension to be roughly $10^{-11}$N, in good agreement with the theoretical calculation [59].

The theoretical descriptions mentioned above have been successfully used to model the binding energy of micro-sized particles at WO interfaces. It is difficult to deduce the line tension by measuring the contact angle at a microscopic scale by Eq. 1.2, because the interface and contact line may be shifted from the horizontal plane. As an alternative, the wettability of nanoparticles at interfaces has been calculated by molecular dynamics or Monte Carlo simulations. Recent simulation studies have reported that such macroscopic descriptions was also accurate to describe the contact angle of nanoparticles (with size of 1.5nm) at liquid-liquid interfaces[60], while others indicated that these description may underestimate the strength and range of interaction between liquids and particles[17, 61, 62].

Although the water-oil interface possesses certain hydrophobic features, charged homogeneous particles can also be stabilized at WO interfaces, provided the surface charge is low[63, 64]. Two common ways are available to decrease a charge on nanoparticle surface: (1) by decreasing/increasing the pH in aqueous phases for negative/positive charged nanoparticles or (2) by decreasing the number of the charged chemical groups by chemical reactions. But for "big" charged nanoparticles ($R$ >8nm), Wang Et al. did not observe detachment at a water-heptane interface[63].

## 1.2.3 Stability of Janus particles at water-oil interfaces

The term "Janus" denotes a type of particles which have two or more different surface regions. An example is a particle with one side having the polar properties and the other side possessing the apolar properties. Janus particles have strong interfacial activity, due to a combination of the amphiphilic feature of surfactants and the physical properties of nanoparticles. This feature opens new opportunities for Janus nanoparticles in the areas of nanoparticle assembly and emulsion stabilization [65]. For example, Glaser et al. reported a significant decrease in interfacial tension for a hexane-water interface suspended with Janus nanoparticles. In their work, a Janus nanoparticle consisted of a gold particle with diameter of 4nm, adhering to a 10nm iron oxide particle. The amphiphilicity could be obtained by ligand exchange with dodecanethiol or octadecanethiol on the gold particle[66].
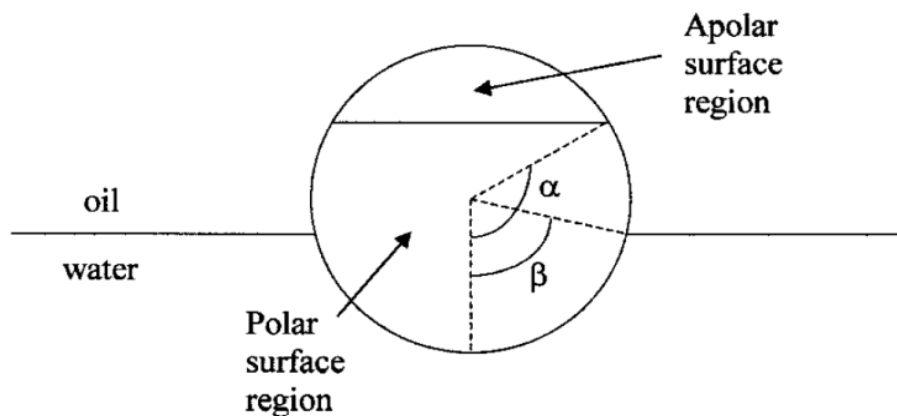


*Figure 1.8* *A scheme of a Janus particle at a water-oil interface. The ratio of polar and apolar region is determined by angle α. Angle β indicates the immersion of the particle at a WO interface. This picture is reprinted from ref.* [67].

The desorption energy of Janus particles at liquid-liquid interface is calculated as follows. As shown in Fig.1.8, angle $\alpha$ indicates the ratio between the polar and apolar region. Angle $\beta$ indicates the immersion of a particle at a WO interface. The desorption energy $E$ of Janus particles at a WO interface can be given by [67]

$$E(\beta) = 2\pi r^2 [\gamma_{OA}(1+\cos\alpha) + \gamma_{OP}(\cos\beta - \cos\alpha) + \gamma_{WP}(1-\cos\beta) - \frac{1}{2}\gamma_{WO}(\sin\beta)^2) \quad (\beta \leq \alpha) \quad (1.6)$$

$$E(\beta) = 2\pi r^2 [\gamma_{OA}(1+\cos\alpha) + \gamma_{WA}(\cos\alpha - \cos\beta) + \gamma_{WP}(1-\cos\beta) - \frac{1}{2}\gamma_{WO}(\sin\beta)^2) \quad (\beta \geq \alpha) \quad (1.7)$$

Here, $\gamma_{WA}$, $\gamma_{OA}$, $\gamma_{WP}$ and $\gamma_{OP}$ refer to the interfacial tension of apolar-water, apolar-oil, polar-water and polar-oil interfaces, respectively. A Janus particle attached on an interface could be characterized by two contact angles: the contact angle of the apolar region $\theta_A$ and polar region $\theta_P$. The determination of $\theta_A$, $\theta_P$ and $\theta_{average}$ can be given by Young's equation,

$$\cos\theta_A = -\frac{\gamma_{WA} - \gamma_{OA}}{\gamma_{WO}},$$

$$\cos\theta_P = -\frac{\gamma_{WP} - \gamma_{OP}}{\gamma_{WO}}$$

$$\theta_{average} = -\frac{\theta_A(1+\cos\alpha) + \theta_P(1-\cos\alpha)}{2}$$

$$\text{(1.8)}$$

Angle $\beta$ always corresponds to the lowest surface energy configuration. Thus, angle $\beta$ can be described in different situations,

$$if\, \alpha < \theta_P < \theta_A, \beta = \theta_P;$$

$$if\, \theta_P < \alpha < \theta_A, \beta = \alpha;$$

$$if\, \theta_P < \theta_A < \alpha, \beta = \theta_A \qquad (1.9)$$

Eqs. 1.6 and 1.7 could be used to calculate the minimum surface energy $E_{min}$ of the attached Janus particles at a WO interface. Fig. 1.9 shows the change of the desorption energy as a function of the average contact angle $\theta_{average}$ for a Janus particle at a WO interface. For the calculation, $\alpha$, $r$ and $\gamma_{WP}$ are set to 90º, 10nm and 36 mN m$^{-1}$, respectively [67]. The symmetric particle corresponds to $\Delta\theta = 0º$. The maximum amphiphilicity is expected to be $\Delta\theta = 90º$ where the polar region is totally wetted in water and the apolar region is completely wetted in oil. In this case, the desorption energy of a Janus particle is approximately four times higher than that of a symmetric particles at $\theta_{average}=90°$.
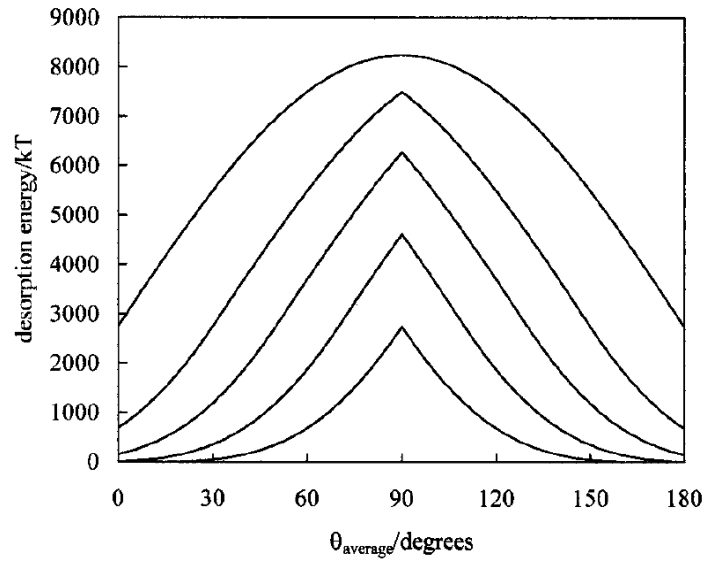


**Figure 1.9** *Variations of the desorption energy vs. the average contact angle $\theta_{average}$, for Janus particles with radius 10 nm and $\alpha = 90º$. The interfacial tension was set to 36 mN m$^{-1}$. In order to tailor the amphiphilicity, the curves refer to $\Delta\theta$ of 0, 20, 40, 60 and 90º (from bottom to top). This picture is reprinted from Ref. [67].*

## 1.2.4 Diffusion of particles at interface: theoretical models

The diffusion coefficient $D$ of particles in a pure viscous fluid depends on the friction coefficient, $f$, by the Einstein expression:

$$D = k_B T / f \tag{1.10}$$

In a three dimensional system $f=6\pi\eta R$ where $\eta$ is the viscosity, $R$ is the particle radius. Thus, in a pure viscous fluid, the viscosity could be obtained by measuring the particle diffusion coefficient. However, in two dimensional systems, the situation is not clear until now. For a disk with radius $R$ moving laterally within a highly viscous membrane with thickness $h$ in an aqueous phase, the motion of the disk leads to a backward flow in the surrounding aqueous phase and also in the membrane. Thus, the diffusion of a disk could be described as follows [68]:

$$1/f = \frac{1}{4\pi\eta_L h}(\ln(\frac{\eta_L R}{\eta_W R} - \xi)) \tag{1.11}$$

Here, $\eta_W$ and $\eta_L$ are the viscosities of the aqueous phase and the membrane, respectively; $\xi$ is the Euler constant. A non-slip boundary condition is assumed at the interface of the aqueous phase and membrane.

The application of the equation above is limited to the case of particle diffusion within a high viscosity membrane. For a particle absorbed at a liquid-liquid interface, if the diffusion conforms to the Einstein relation, then the viscous drag on the particle can be approximated as the sum of contributions from both liquid phases [69-71]. The relative weighting of each contribution is given by the cross-sectional area of the particle with respect to the contact

angle $\Theta$ in that respective phase. Then the dependence of diffusion coefficient on the viscosities of the two phases could be described as [70, 71]:

$$D_A = \left(\frac{kT}{6\pi R}\right)\left(\frac{2\pi}{2\pi\eta_w + (\eta_a - \eta_w)(2\Theta - \sin 2\Theta)}\right) \tag{3.1}$$

Here, $\eta_w$ and $\eta_w$ are the viscosity of aqueous and alkane phases, respectively. $R$ is the particle radius. Such treatment could successfully describe the diffusion of μm- sized particles at water-oil interfaces [72, 73]. However, for the case of a nanoparticle trapped in an incompressible liquid-liquid interface with contact angle of $\theta$, the theoretical description is on the progress [74, 75].

## 1.2.4 Diffusion of nanoparticles at interfaces: experiments

The diffusion of very small nanoparticles ordered in a two-dimensional film at water-toluene interface was measured by Lin et al., using fluorescence recovery after photobleaching and fluorescence loss in photobleaching [76]. The interfacial diffusion coefficient of nanoparticles was four orders of magnitude lower than that in bulk toluene, plausible due to the crowding effect in which the interfacial viscosity was effectively increased. In a different approach, the diffusion coefficient could be calculated in terms of the dynamic interfacial tension. For the low particle concentration ($1.8 \times 10^{-6}$M) in oil phase, the diffusion coefficient is slightly lower than that in bulk [77].
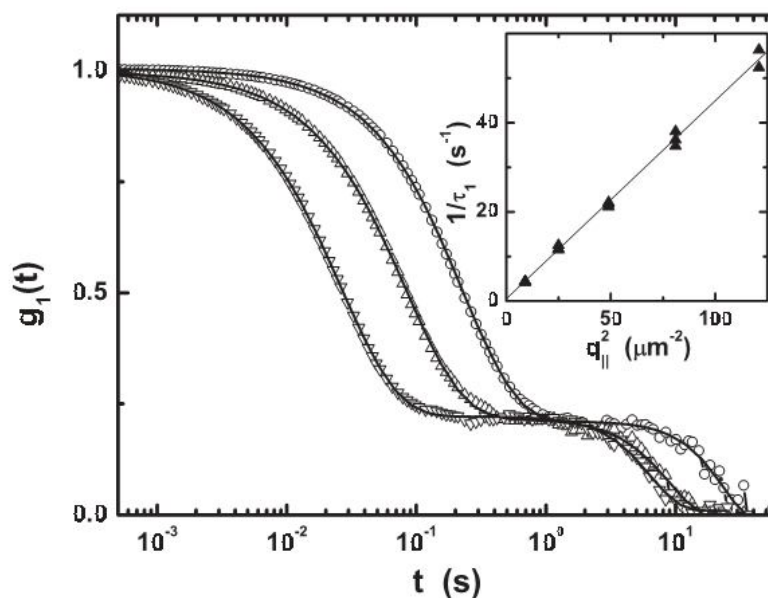
*Figure 1.10* *Autocorrelation functions and the corresponding fits, for polystyrene colloidal particles with radius of 52.3nm at a heptane-water interface, under evanescent-wave illumination with penetration depth $p^{-1}$=2μm. The different symbols indicate different parallel scattering vector. This picture is reprinted from Ref.*[78]*.*

Recently, Stocco et al. reported an evanescent-wave dynamic light scattering study to measure the lateral diffusion of nanoparticles (polystyrene colloid, 52.3nm) at a heptane-water interface [78]. A two-step decay of the autocorrelation function was found, as shown in Fig.1.10. Remarkably, the interfacial diffusion coefficient appeared roughly an order of magnitude lower than that in bulk water. The author attributed the two-step decay of the autocorrelation function to the hindered diffusion within an interfacial particle lattice, stabilized by repulsive electrostatic interactions.

## 1.3 Summary and Motivation

In this thesis, I investigated the diffusion of molecules and nanoparticles at WO interfaces, using Fluorescence Correlation Spectroscopy (FCS). In the past FCS was already successfully used to study tracer diffusion in complex fluids [79, 80] and at solid-liquid interfaces [81-84], etc. However, it is difficult to adjust the observation volume at a liquid-liquid interface, because of a short working distance of the high-numerical-aperture objective (roughly 200μm away from the glass surface). To the best of my knowledge, this is the first time to trace the diffusion of single objects at planar water-oil interfaces by FCS.

First of all, I measured the diffusion of three fluorescent molecules at WO interfaces which reflected the interface properties on the length scale of the fluorescent tracer's size. As the physical picture of WO interfaces at a microscopic scale is still not clear, I used a new strategy to study this question: I employed fluorescent tracers to "feel" the interfacial properties by detecting the lateral diffusion at WO interfaces. In particular, Rhodamine 6G and PDI**1** molecules with $R_H$=0.6 and 1.0nm exhibited a faster diffusion than that predicted by Stokes-Einstein equation while the interfacial diffusion of a large tracer, water soluble dendrimer, just reflected the surrounding viscosity. These results leaded to the conclusions that a low viscosity layer exists on the length scale of several angstroms at WO interfaces.

Consequently, I studied the diffusion of small nanoparticles at WO interfaces using FCS. The experimental results are presented in the chapter four. Quantum dots with different surface coating were used as model nanoparticles. I first applied FCS to study the interfacial diffusion of hydrophobic nanoparticles at WO interfaces and compared it with the diffusion in bulk. A slowdown of nanoparticle diffusion at WO interfaces was observed. In addition, the effect of surface properties, the particle sizes and the viscosities of the oil phases were studied.

Because this was the first time to that diffusion of single nanoparticles at interfaces has been studied, a series of artifacts were ruled out. Especially, since there is a strong tendency for nanoparticles to self-assemble at WO interfaces, the measurements should be conducted at a very low surface coverage. Therefore, FCS offers a great advantage because it is possible to carry out a measurement at an extremely low surface coverage (usually ~ more than 1 $\mu m^2$).

In the last section of chapter 4, the interfacial diffusion of Janus nanoparticles at WO interfaces was investigated. The Janus nanoparticles had significantly higher interfacial activity compared to their symmetric counterparts, and thus attracted considerable attentions. Although it was well known that the presence of Janus nanoparticles can abruptly decrease the interfacial tension, little was known about the dynamic of Janus nanoparticles at WO interfaces. Here, I carried out a comparative study to investigate the difference of the interfacial diffusion of symmetric and Janus nanoparticles by varying the viscosity of both immiscible liquid phases and by adjusting the interfacial tension. The results could be helpful to understand the interfacial activity and to even rational design the Janus nanoparticles on demand.

# CHAPTER 2

## Materials and methods

### 2.1 Principle of fluorescence correlation spectroscopy (FCS)

FCS is a promising technique to study the mobility of small fluorescent tracers in liquid phases at a single particle level. The mobility information is obtained by monitoring and analyzing the fluorescence fluctuation caused by fluorescent tracers coming in and out of a small observation volume $V$. This technique was firstly reported by Madge, Elson and Webb in the early 1970s [85, 86] to study the chemical kinetic of DNA-drug intercalation and was consequently improved by a combination with the confocal illumination-detection system in the middle of 1990s [87]. Such improvements allowed a combination of high precision and low background noise, arousing renewed attention. By now FCS is a wide-used technique to study the polymer conformational fluctuations, the molecular interactions, the kinetic of chemical reactions and molecular diffusion in confinement, etc.

A typical FCS setup is illustrated in Fig.2.1. In an inverted microscope, a laser beam is directed by a dichroic mirror onto the back-aperture of a high numerical aperture (NA) objective (usually NA>0.9) and strongly focused into the studied sample. The red-shift fluorescence from the sample is collected by the same objective and passes through the dichroic mirror, the emission filter, the confocal pinhole and finally reaches the detector, typically an avalanche photodiode (APD). A confocal pinhole with tunable diameters (30-120μm) in an image plane blocks the out-of-focus fluorescence and as such, provides sufficient axial resolution. Thus a so-called observation (or detection) volume is created. Only

the fluorescence from tracers that are in this volume can be detected. The profile of the observation volume could be described as an ellipsoidal shape with axial and radial length $r_0$ and $z_0$, located in the middle of the focused laser beam with the intensity in a Gaussian distribution. In a typical measurement in bulk water, $r_0$ and $z_0$ are roughly 0.2 and 0.6 μm, respectively, as shown in Fig.2.1.
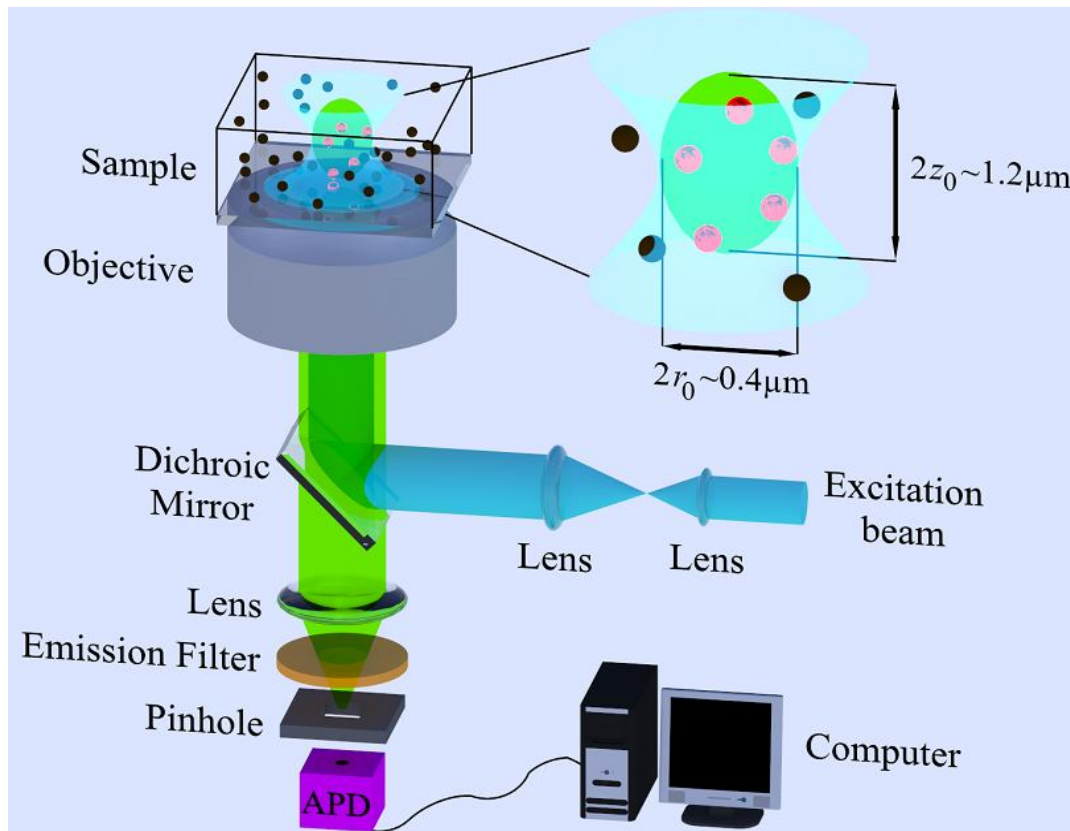


*Figure 2.1 A scheme of a fluorescence correlation spectroscopy (FCS) setup. This picture has not been scaled. A magnified image of the focused laser to illustrate the laser intensity distribution (cyan) and the observation volume (green) in the samples is shown on the right side of this picture. This picture is kindly offered by Stoyan Yordanov.*

Herein, I review the basic theory and explain how FCS works. As the fluorescent species diffuse through the observation volume, they result in the fluorescence fluctuations, $\delta F(t)$ (Fig.2.2), which is described as the deviation from the average intensity $<F>$.

$$\delta F (t) = < F > - F (t) \qquad (2.1)$$
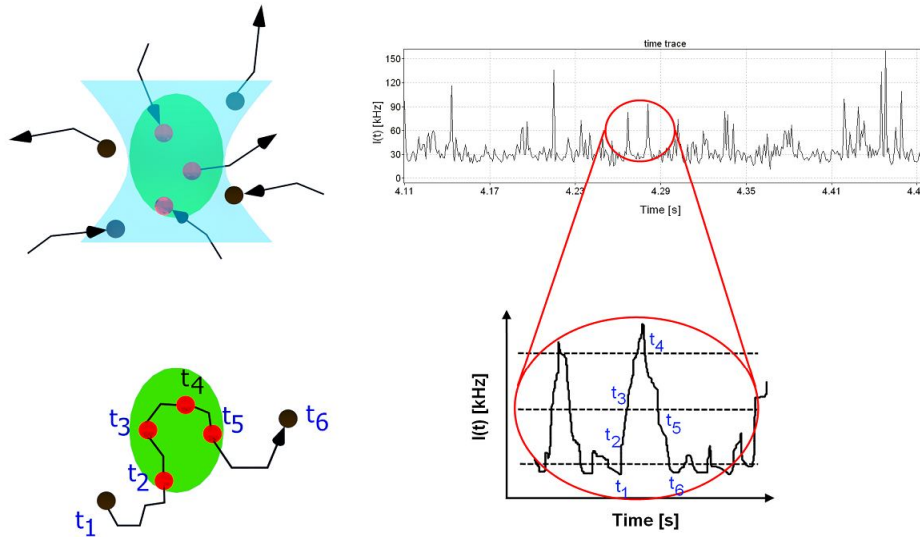


***Figure 2.2*** *Fluorescence fluctuations caused by diffusing fluorescent species coming in and out of the observation volume. This picture is kindly offered by Stoyan Yordanov.*

Then the autocorrelation function for the intensity divided by average intensity squared could be defined as,

$$G(\tau) - 1 = \frac{< F(t)F(t + \tau) >}{< F(t) >^2} \qquad (2.2)$$

The autocorrelation function corresponds to the probability that a fluorescent molecule in the detecting volume $V$, at a time $t$, will still be within the detecting volume at a time $t + \tau$.

35

Theoretically, the fluctuation $\delta F(t)$ arising from the local concentration change of fluorescent species in the observation volume $V$, can be represented as [88],

$$\delta F(t) = \int_V W(r) \bullet \delta(Q \cdot C(r,\tau)) \cdot dV \tag{2.3}$$

Here, the term $Q$ refers to the quantum yield and detector efficiency. The term $\delta C(r)$ represents the concentration fluctuation in the detecting volume due to the diffusion of fluorescent species. Finally, $W(r)$ represents the observation volume estimated by three-dimensional Gaussian detection profile as follows:

$$W(r) = e^{-2\frac{x^2+y^2}{r_0^2}} \bullet e^{-2\frac{z^2}{z_0^2}} \tag{2.4}$$

Inserting the Eqs.2.3 and 2.4 into Eq.2.2 and carrying out an integration, for one-component diffusion the autocorrelation curves could be represented as follows [88],

$$G(\tau) - 1 = \frac{1}{N} \frac{1}{[1+t/\tau_D]\sqrt{1+\frac{t}{S^2\tau_D}}} \tag{2.5}$$

Here, $\tau_D$ is diffusion time and represent the average time that the fluorescent species need to cross laterally the observation volume. $S$ is the structure parameter, $S=z_0/r_0$ where $z_0$ and $r_0$ indicate the axial and radial length of the elliptical observation volume. $N$ is the average number of fluorescent species in the observation volume. Then the diffusion time $\tau_D$ is related to the diffusion coefficient $D_{bulk}$,

$$D_{bulk} = x_0^2/4 \ \tau_D \tag{2.6}$$

The application of FCS is not only limited in three dimensional systems. Lots of studies have been done to focus on the diffusion of fluorescent species in two dimensional systems, e.g., in lipid membranes or at solid-liquid surfaces. In a two dimensional system, the observed detecting volume can be evaluated by a planar two dimensional Gaussian distribution,

$$W(r) = Ae^{-2\frac{x^2+y^2}{r_0^2}}$$

(2.7)

Inserting the Eqs.2.3 and 2.7 into Eq.2.4 and carrying out an integration, then the autocorrelation function for one-component diffusion in two dimensions can be rewritten as,

$$G(\tau) - 1 = \frac{1}{N} \frac{1}{[1 + t / \tau_D]}$$

(2.8)

The diffusion coefficient can also be given as $D_{\parallel} = x_0^2/4\tau_D$.

## 2.2 FCS experimental setup

The measurements described in this thesis were carried out on a commercial FCS setup comprising of the module ConfoCor2 and an inverted microscope (Axiovert 200, Carl Zeiss, Jena, Germany), a laser unit and an avalanche photo diode detector, as shown in Fig.2.3. A C-Apochromat 40x/NA1.2 water immersion objective with Milli-Q water (resistivity of 18.2 MΩ·cm) as the immersion liquid were used in chapter 3 and the last section of chapter 4 while a 40x/NA0.9 Plan Neofluar objective with glycerol as the immersion liquid was used in section 4.1 and 4.2.

An Ar laser (488nm) was used to excite the diffusing fluorescent species. The emissions were collected by the same objective. After passing through a LP530 long pass emission filter and a confocal pinhole, the fluorescence finally reached an avalanche photodiode detector. Then fluorescence fluctuations recorded were correlated by the Zeiss software.



*Figure 2.3* *A picture of FCS setup.*

## 2.3 Interfacial tension measurement

All the interfacial tension measurements reported in this thesis were performed using software controlled Du-Noüy ring tensiometer (ring height = 25mm, ring diameter =18.7mm and wire thickness = 0.37mm), as shown in Fig.2.4. Du-Noüy ring tensiometer measured the surface/interfacial tension by using a standardized ring with a ring/plate tensiometer. The ring was immersed into the liquid and then drawn out. This formed a liquid lamella that was stretched to its maximum. Samples were measured in a 50 cm$^3$ measuring cell at a temperature of 293 ± 0.5 K. Platinum-Iridium ring was flame-dried before each experiment. The ring hanging from the balance hook was immersed just below a liquid-liquid interface and was pulled upwards slowly. This caused the denser liquid film to stretch and the maximum force experienced was recorded. This force was directly related with the interfacial tension along with the densities of the liquids. The surface/interfacial tension could be calculated by,

$$\gamma = F / 2\pi(R_1 + R_2) \tag{2.9}$$

Here, $F$ is the detachment force and $R_1$, $R_2$ are the inner and outer radii of the ring. The constant 2 takes into account the inner and outer diameter of the ring. In this thesis, each value was an averaged value of 10 measurements with an accuracy of ± 0.05 mN/m.

***Figure 2.4*** *A picture of Du-Noüy ring tensiometer.*

## 2.4 Materials

Water

Water used for the sample preparation and cleaning was Milli-Q water with resistivity of 18.2 MΩ·cm, prepared by a Sartorius Arium611VF water purification system.

Glycerol

Glycerol was commercially purchased from Sigma-Aldrich without further purification. Because of its high viscosity and good miscibility with water, glycerol was utilized here to control the viscosities of the aqueous phases.

n-Alkane

All the *n*-Alkanes used in this thesis, i.e., *n*-hexane, *n*-octane, *n*-decane, *n*-dodecane, *n*-tetradecane and *n*-hexadecane were purchased from Sigma-Aldrich. *n*-dodecane was also obtained from Fisher Scientific Co. The purity of the alkane was promoted by a facile method in which the surface active solutes were removed at the location of their enrichment [89]. The "interface-chemical" purity could be evaluated by measuring the interfacial tension, as tabulated in Tab.2.1. For comparison I also plotted previously reported data, consistent well with these I measured. This was a good evidence to confirm the purity of the interfaces that I used.

***Table 2.1*** *Interfacial tension of various water-alkane interfaces  (T=20°C)*

| n-alkane | γ (water/*n*-alkane) (mN/m) (in Ref. [90]) | γ (water/*n*-alkane) (mN/m)[a] |
|---|---|---|
| hexane | 50.80 | 49.65 |
| octane | 51.64 | 50.56 |
| decane | 52.33 | 51.36 |
| dodecane | 52.87 | 51.69 |
| hexadecane | - | 52.42 |

Surfactant and salt

The surfactant and salt were only used in control experiments. The surfactant used was sodium dodecyl sulfate (SDS) and cetyltrimethylammonium bromide (CTAB), used as received. The salt utilized was potassium chloride, which was also used as received.

Rhodamine 6G

The Rhodamine 6G was purchased from Sigma-Aldrich. Rhodamine 6G was utilized in chapter 3. The molecular weight is 479.02 g/mol. The chemical structure is shown in Fig.2.5. Fig.2.6 shows the optical properties of Rhodamine 6G in bulk water.
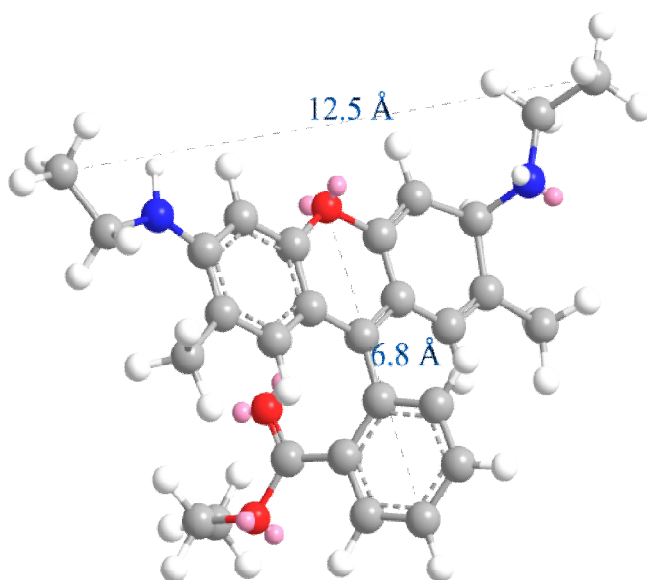


**Figure 2.5** *Chemical structure of Rhodamine 6G. The red, blue, gray and white spheres represent the oxygen, nitrogen, carbon and hydrogen atoms, respectively.*
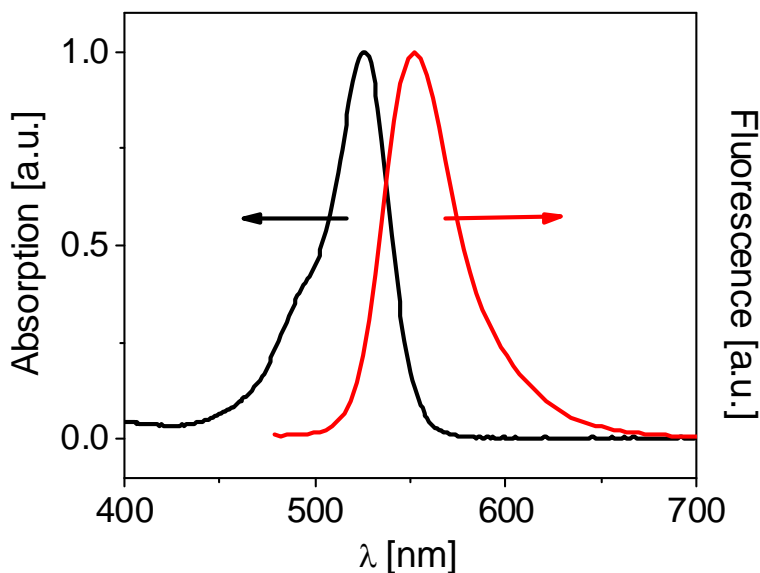
***Figure 2.6*** *Normalized absorption and emission spectra of Rhodamine 6G in bulk water.*

Dendrimer

The PDI-G1-PAEMA dendrimer was synthesized and purified following a previously published procedure [91]. It was constructed from a fluorescent perylenediimide chromophore core surrounded by a hydrophobic polyphenylene shell as the first layer and a flexible water soluble poly(aminoethyl methacrylate) (PAEMA) shell as the second layer. Fig.2.7 shows the chemical structure. Each PAEMA chain has 12-13 monomer units as estimated from $^1$H-NMR of the tert-butyloxycarbonyl (BOC)-protected precursor PDI-G1-BOC-AEMA. Gel permeation chromatography (GPC) of the precursor in dimethylformamide gave a $M_n$ = 19.8kDa, a $M_w$ = 23.5kDa and a polydisperisty index of 1.19 using a UV detector and PS as a standard. Fig.2.8 shows the optical properties of dendrimers in bulk water.
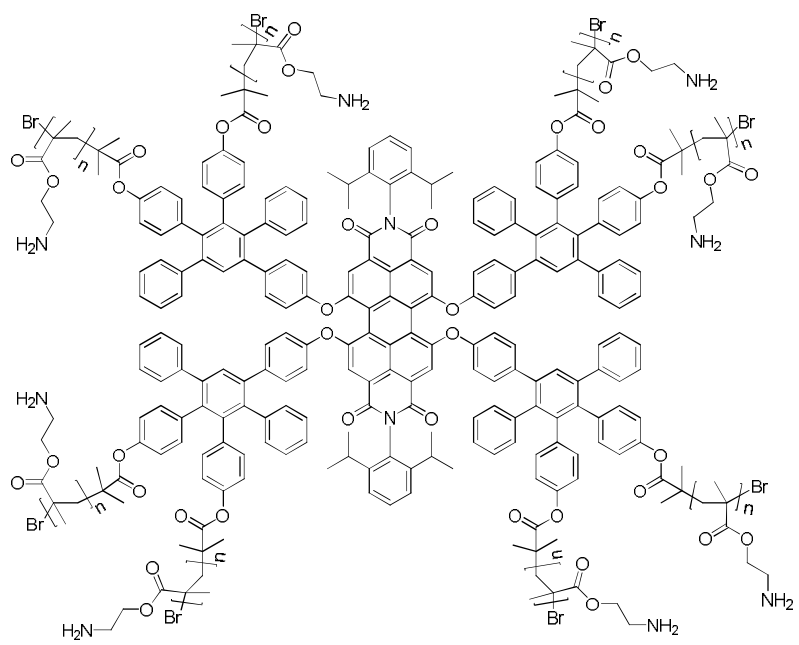
***Figure 2.7*** *Chemical structure of a dendrimer molecule.*
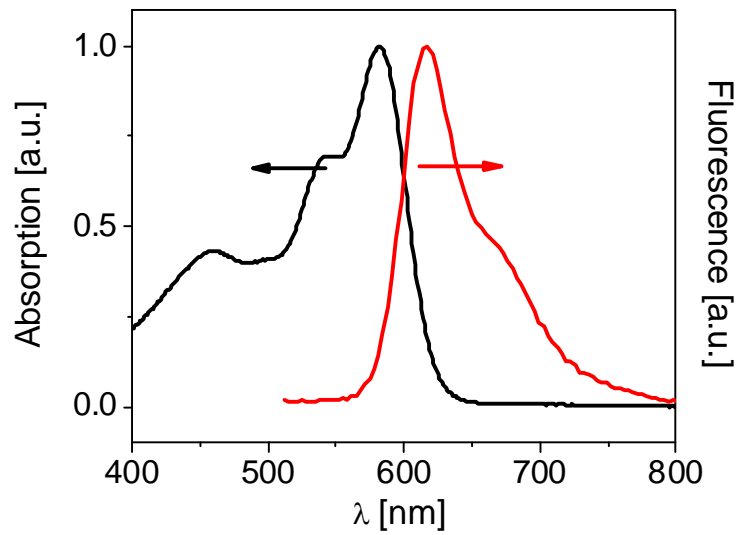


***Figure 2.8*** *Normalized absorption and emission spectra of dendrimers in bulk water.*

<u>Water soluble perylene</u>

The water-soluble perylene dye referred as PDI**1**, was prepared as described previously [92]. It possesses a negative charge. The chemical structure is shown in Fig.2.9. Fig.2.10 shows the optical properties of PDI**1** in bulk water.



***Figure 2.9*** *Chemical structure of a PDI1 molecule.*



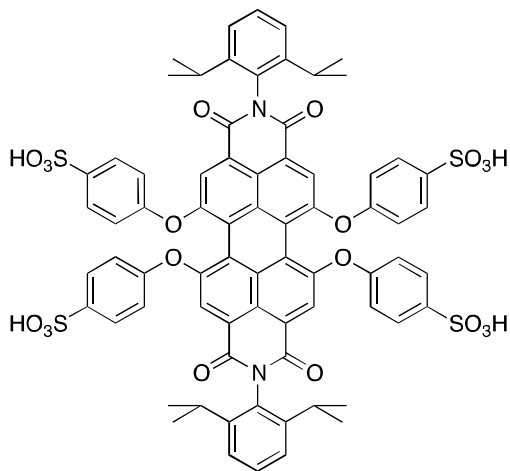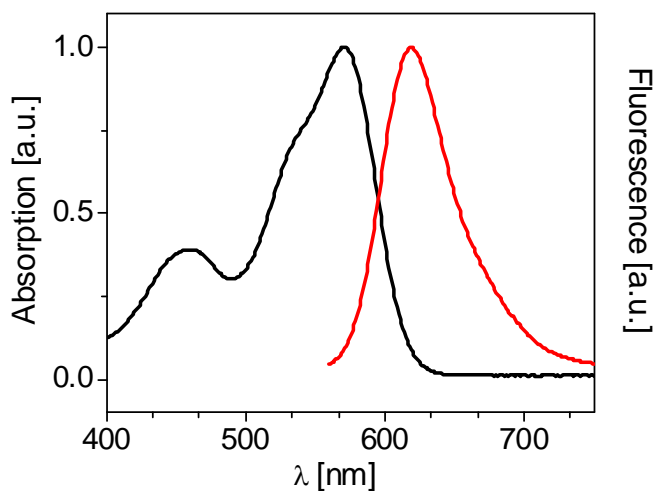***Figure 2.10*** *Normalized absorption and emission spectra of PDI1s in bulk water.*

## Symmetric nanoparticles

The quantum dots were used as model NPs in this thesis. The symmetric QDs were purchased from Invitrogen in a suspension state (8μM in borate buffer, concentration = 0.05M and pH = 8). They were coated with amphiphilic polymer layers, which attach carboxylic groups on the surface. This provides an electrostatic charge to prevent aggregation in bulk water. The organic quantum dots with hydrophobic surface were also purchased from Invitrogen. The quantum dots were dispersed in bulk decane with a concentration of 1μM.

## Janus nanoparticles

The Janus and symmetric NPs discussed in the last section of chapter 4, were kindly provided from C. Li /Uni. Drexel. They were prepared by specific functionalization of CdSe based quantum dots (QD). To obtain Janus NPs, these QDs were functionalized with one hemisphere of the polyethylene glycol, and the other hemisphere with twelve-carbon alkane. For the symmetric NPs, the surface of QDs was functionalized with the polyethylene glycol only. Both types of the quantum dots were dispersed in dichloromethane. The Janus nanoparticles were prepared by a combining "solid-state grafting-to" and "grafting-from" method, as shown in Fig.2.11. The procedure was given as follows[93, 94]. Briefly, the polyethylene oxide was solution crystallized into lamellar single crystals on a solid surface (Fig.2.11b). QDs with ammonium-ligand on the surface were then placed on the crystal surface (Fig.2.11c). Then dodecanthiol was replaced with the ammonium-ligand on the top surface of QDs (Fig.2.11d).
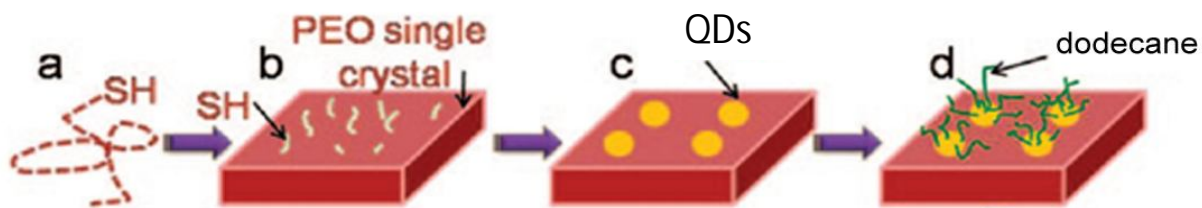
***Figure 2.11*** *Cartoon of Janus nanoparticles functionalized by a combining "solid-state Grafting to" and "Grafting-from" method. This picture is reprinted from Ref.* [94].

## 2.5 Sample preparations

In this part I describe the approach that was used to construct a water-oil interface suspended with fluorescent tracers. An Attofluor cell chamber (Invitrogen, Leiden, Netherlands) and a glass slide with 25mm in diameter and 0.15mm in thickness were used as a sample cell. An alumina ring was glued on the glass slide to form a small cell to constrain the aqueous solutions, as shown in Fig.2.12.



***Figure 2.12*** *An Attofluor cell chamber with an alumina ring.*

To build a water-oil interface, (i) a defined amount (approximately 5~15 μL) of aqueous solution was added into the measuring cell; (ii) a drop of 0.5~4 μL of tracer´s dispersion with a concentration of $10^{-10}$M, was dropped upon the pure aqueous phase; (iii) roughly 80~200 μL of alkanes were carefully added on top of the liquid surface. The tracer molecules or particles were totally absorbed at interfaces. (iv) This was confirmed by shifting the objective in vertical direction through the sample with 100~200 nm for each step and thus scanning the FCS observation volume through the interface. As shown on Figure 2.13 strong fluorescence signal was obtained only when the observation volume was crossing the interface. Consequently, the FCS observation volume could be precisely located in the middle of a WO interface by adjusting to the point of maximum intensity. The schematic presentation of how FCS measures the diffusion of fluorescent species at a planar WO interface is shown in Fig.2.13.

(b)
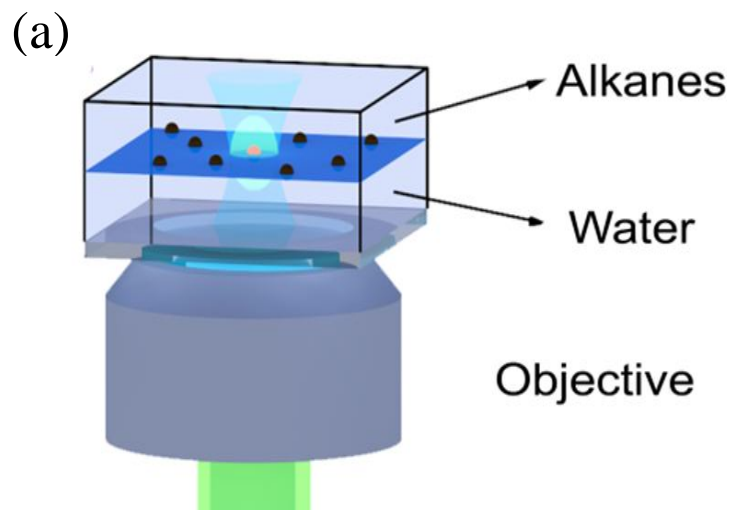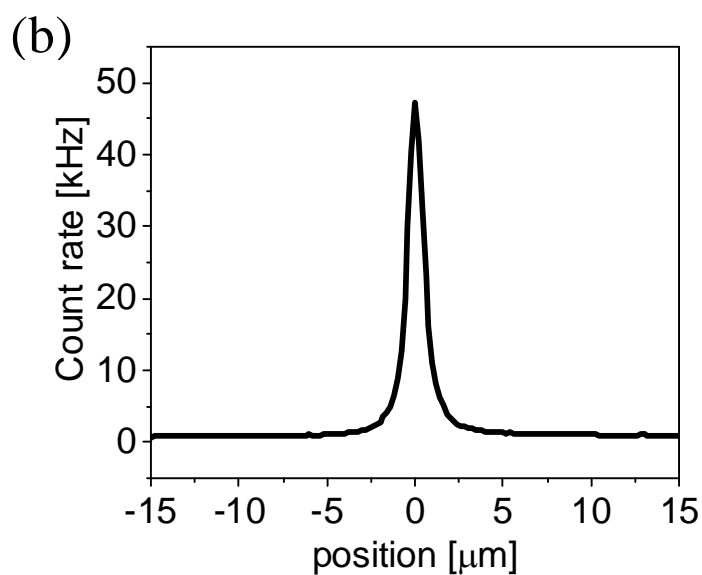


*Figure 2.13* (a) A Scheme of how FCS measures the diffusion of fluorescent species at a WO

interface. The blue plate indicates an interface between water and alkanes. The black spheres

indicate the fluorescent species suspended at interfaces. The observation volume (bright cyan)

was precisely adjusted at the middle of an interface. A fluorescent tracer is excited (pink

sphere) in the observation volume. (b) A typical fluorescence intensity scanning through a

water-decane interface on which Rhodamine 6G is adsorbed.

# CHAPTER 3

## A Reduced viscosity layer at water-oil interfaces

In this chapter, I applied the technique of fluorescence correlation spectroscopy (FCS) [95] to study the diffusion of tracer molecules with different sizes at water/$n$-alkane interfaces and probe the properties of WO interfaces on the length scale of tracer's size. Compared to other techniques, FCS is well suited for such studies as it offers the possibility to monitor sub-nanometer size objects with high mobility at a very low surface coverage[95].

At the first part of this chapter, I described a calibration protocol allowing accurate determination of the absolute values of the interfacial diffusion coefficient $D_{//}$. Then I studied $D_{//}$ of water soluble, fluorescent core-shell dendrimer molecules with a hydrodynamic radius of $R_H = 4.0$ nm as a function of the viscosity of both liquid phases. The size of dendrimer molecules is much bigger than the width of a WO interface. Therefore, the interfacial diffusion was not affected by specific interface properties and simply reflected the bulk viscosities of the surrounding aqueous and oil phases. Afterwards, the interfacial diffusion of Rhodamine 6G and PDI**1** with relatively small $R_H$ (0.6 and 1.0nm respectively) was studied. A fast diffusion, compared to what can be expected from the bulk viscosity values of the surrounding phases was observed. This indicated the existence of a very thin layer (on the length scale of several angstroms) with a reduced viscosity at water-alkane interfaces.

## 3.1 Calibration of FCS observation volume at water-oil interfaces

As the lateral dimension of the confocal detection volume depends on the geometrical characteristics of the optical setup and the refractive index ($n_S$) of the sample, an appropriate calibration is necessary. Typically this is done by measuring the autocorrelation curves of a freely diffusing dye molecules with known diffusion coefficient, e.g. Rhodamine 6G in water. In the case of diffusion at a WO interface, the procedure is not straightforward. Indeed, while the calibration is done in pure water, during the 2D measurements the focus is partially positioned in the alkane phase, which has a higher refractive index than water. This may cause optical distortions which result in a small change in the lateral dimension of the observation volume. Consequently, this gives rise to a systematic error in the estimated values of the interfacial diffusion coefficient, $D_{//}$.

A recent simulation [96] showed a comparison between the observation volume in bulk water and that at a WO interface, as shown in Fig. 3.1. The observation volume in bulk water exhibited a nicely elliptical shape while that at a WO interface showed a scattering pattern. Most notably, the simulated $r_0$ at WO interfaces which was rough 230nm, was similar to an experimental value in bulk water, 237nm obtained by measuring the diffusion time of Rhodamine 6G and using its diffusion coefficient value, $3.82 \cdot 10^{-10}$ m$^2$/s at 22°C that is known from independent measurements with multi-color dual-focus fluorescence correlation spectroscopy [97].

With regard to my study, the molecular tracers were only suspended at WO interfaces and no fluorescence could be detected in the bulk, lending credence to the fact that the likely scattering feature in the bulk region did not influence the lateral dimension of the observation volume at WO interfaces (Fig.3.1).
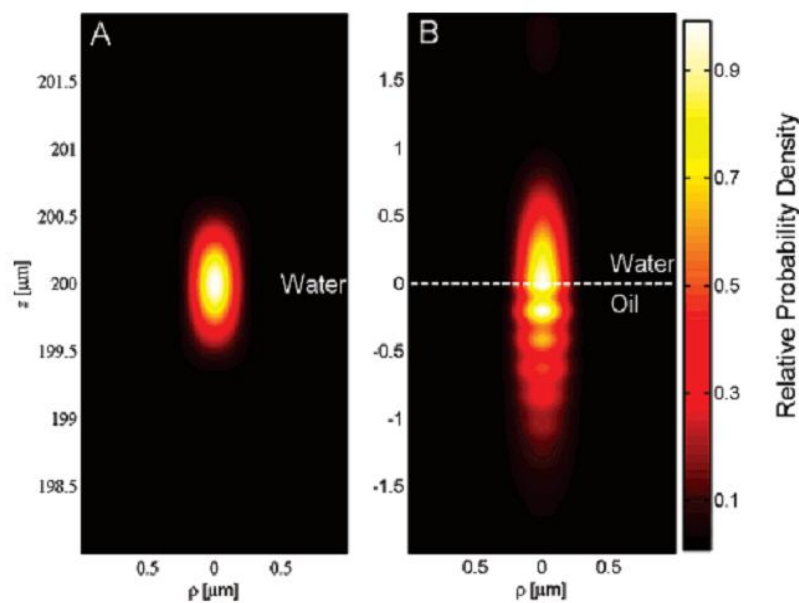
***Figure 3.1*** *Simulation results of the FCS observation volume in (A) bulk water and (B) at a*

*WO interface. The focus intensity is shown in pseudo color. This picture is reprinted from Ref.*

[96].

Furthermore, as the different alkanes have slightly different refractive indices, the eventual error may depend on the alkane length. In order to estimate the magnitude of these effects I have measured the diffusion time of organic quantum dots (Invitrogen, Leiden, Netherlands) with hydrodynamic radius of 5.0 nm in all alkanes, using the same water immersion objective as for the 2D studies, and plotted it against the alkane viscosities, as shown in the Fig.3.3. The solid line shown in the figure represents the value of the diffusion time calculated on the basic of the Stokes-Einstein equation assuming the same lateral dimension of the observation volume for all alkanes used. As can be seen there is a remarkable agreement between the experimental data and the prediction based on the Stokes-Einstein equation [95, 98]. Thus, the results presented in Fig. 3.2 show that changing the

refractive index from 1.37 for hexane to 1.43 for hexadecane has only a minor effect (less than 5%) on the size of the observation volume. As the water refractive index 1.33 is only slightly smaller than that of hexane I estimate that the error in the calibration of the lateral dimension of the observation volume is less than 10%. I conclude that even if optical distortions cause systematic error in the estimated values of the interfacial diffusion coefficient, this error is small and does not depend on the carbon number of alkanes.
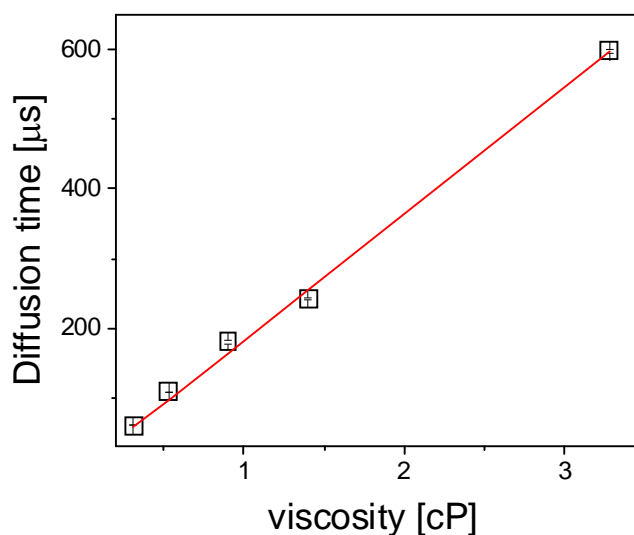


***Figure 3.2*** *Diffusion time of quantum dots with $R_H$ =5.0 nm in bulk alkanes as a function of the viscosity of alkanes; the red, solid line represents the prediction of the Stokes-Einstein equation.*

Thus, in this thesis, the calibration was done by measuring the diffusion of a standard water soluble dye, Rhodamine 6G, with diffusion coefficient of $3.82 \cdot 10^{-10}$ m$^2$/s at 22°C in bulk water. Fig. 3.3 shows a typical autocorrelation curve of Rhodamine 6G in bulk water. The experimental curve can be nicely fitted by Eq.2.5, yielding a diffusion time of $\tau_D$ = 28~30

μs, and S = 5~6. Based on these data, $r_0$ can be calculated by $r_0^2=4\tau \cdot D$ and a value of 0.22μm is obtained.
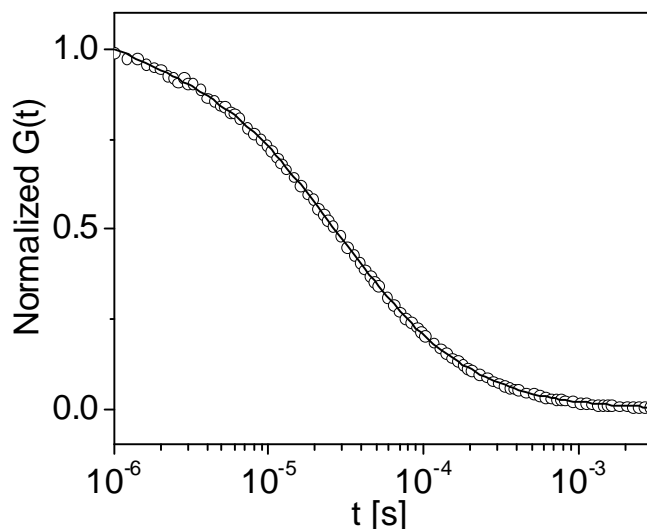


***Figure 3.3*** *A typical autocorrelation curve of Rhodamine 6G in* bulk water.

## 3.2 Procedure to build the water-oil interfaces suspended with molecular tracers

In this chapter I used degassed liquids to perform all the measurements. To degas the liquids, Milli-Q water and alkanes after equilibration with atmospheric air (in Mainz, Germany, elevation is 85 - 285 m) were subjected to vacuum degassing. Vacuum was applied to liquid flasks with a Teflon stirrer. Continuous stirring was used to shake off the bubbles nucleated on the surface of the Teflon stirrer. The system was kept under vacuum for more than 2 hours until no bubble formation was seen on the Teflon stirrer [35].
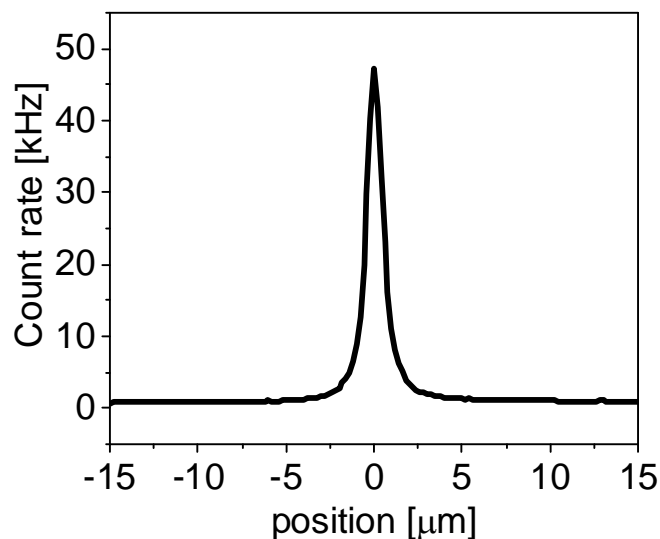
***Figure 3.4*** *A fluorescence intensity scanning through a water-decane interface on which*

*Rhodamine 6G is adsorbed. Scanning was carried out by moving the focus from water into*

*the alkane phase in steps of 200 nm.*

As described above (section 2.2), to prepare water-alkane interfaces first the sample cell, was filled to a height of 100 µm with a degassed aqueous phase. Then a drop of 0.50 µL aqueous solution of the fluorescent tracers with a concentration of $10^{-11}$ M was added. Finally, a degassed alkane phase was carefully added on top of the aqueous phase. The tracer molecules absorbed fast on the interface, as shown in Fig.3.4. No any fluorescence can be detected in the bulk phases (Fig.3.4). Based on preparation conditions and direct FCS measurements at the interface (see below) I estimate a typical surface coverage of 0.5 $\mu m^2$ per molecule.

## 3.3 Dendrimers at water-oil interfaces

In this part I studied the diffusion of water soluble dendrimers with $R_H$=4.0nm at aqueous-alkane interfaces [95]. Typical autocorrelation curves measured for the dendrimers diffusing at various water-alkane interfaces are shown in Fig. 3.5. The values of the interfacial diffusion coefficients $D_{//}$ obtained for dendrimers at all studied water-alkane interfaces are plotted vs. the alkane viscosity in Fig.3.6. For the dendrimer tracers a gradual decrease of $D_{//}$ with the increase of the alkane viscosity $\eta_a$ was observed.
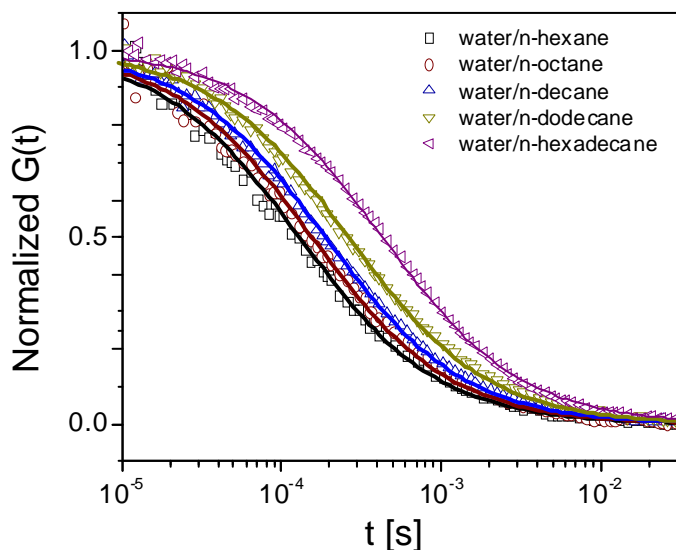


***Figure 3.5*** *Normalized autocorrelation curves of dendrimers diffusing at various water-alkane interfaces and the corresponding fits with Eq.2.5 (solid lines).*
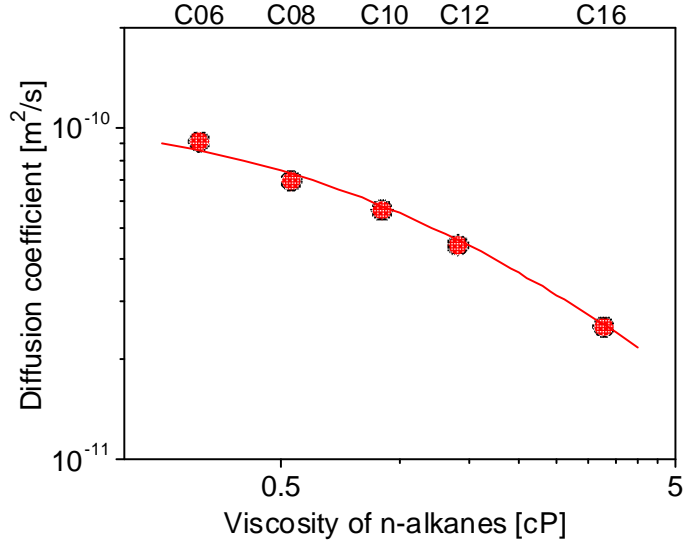
***Figure 3.6*** *Interfacial diffusion coefficient $D_{//}$ vs. viscosity of the alkane phases measured for dendrimers at various water-alkane interfaces. The continuous line is a fit with Eq.3.1 using $R_H$=4.0 nm and $\Theta$=90°. The Cj on the top of the figure indicates the carbon number of the alkane used. The error bars evaluated from the statistical deviations of the measurements are smaller than the symbol size.*

I model the diffusion of the tracer molecules by treating them as spherical particles that obey the Stokes-Einstein relation for diffusion along the liquid-liquid interface [70,71] (Fig.3.7). Then the viscous drag on the sphere can be approximated as the sum of contributions from the water and the alkane phases. The relative weighting of each contribution is given by the cross-sectional area of the sphere in that respective phase (Fig.3.7). The position of the three-phase contact line is characterized by the contact angle $\Theta$. The cross-sectional area of the sphere in the alkane phase is $A_a = R^2(2\Theta - \sin2\Theta)/2$, and that in

the water phase is $A_w = \pi R^2 - A_a$. With this simple model I can estimate the dependence of the diffusion coefficient on the viscosities of the two phases:

$$D_A = \left(\frac{kT}{6\pi R}\right)\left(\frac{2\pi}{2\pi\eta_w + (\eta_a - \eta_w)(2\Theta - \sin 2\Theta)}\right) \tag{3.1}$$

In Eq.3.1 the contributions of the water and alkane are according to their respective cross-sectional areas in the two phases. The contact angle $\Theta$ represents the position of the three-phase contact line of particles at a WO interface. I used $R_H$ as the particle radius $R$ in this work. The experimental results could be fitted well with Eq.3.1 using a contact angle of $(90\pm2)°$ and a hydrodynamic radius of $R_H = (4.0\pm0.1)$ nm in both cases; the error considers only the statistical error of the fitting procedure. In the particular case of a water-decane interface, where the viscosities of the two phases, $\eta_w = 0.96$ cPa s for water and $\eta_a = 0.90$ cPa for decane, are very similar, the value of $D_{//}$ was equal to the diffusion coefficient of $5.6\times10^{-11}$ m$^2$/s (corresponding to $R_H = 4.0$ nm) measured in bulk water.
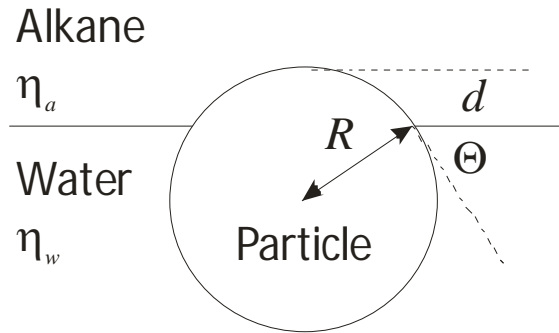


**Figure 3.7** *A scheme of a spherical particle at a water/n-alkane interface. The cross-sectional areas in the alkane and water phase are $A_a = R^2 (2\Theta - \sin 2\Theta)/2$ and $\pi R^2$-$A_a$, respectively, with $\Theta$ in rad.*

To get further insight I also measured $D_{//}$ of the dendrimers vs. the viscosity of the polar (aqueous) phases (Fig. 3.8). The viscosity was adjusted by adding different amounts of glycerol. $D_{//}$ can be described by Eq.3.1 using the same $R_{\mathrm{H}}$ of 4.0 nm and the same contact angle of 90° again. This observation is readily explained by an almost equal immersion of the large dendrimer molecules in the aqueous and alkane phases. Our results is in good agreement with previous observations [99].
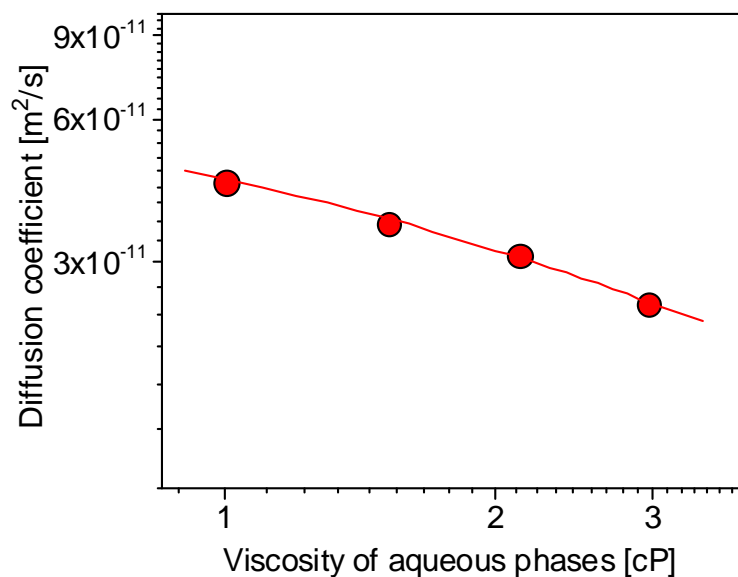


***Figure 3.8*** *Interfacial diffusion coefficient $D_{//}$ vs. viscosity of the aqueous phases for dendrimers at aqueous/dodecane interfaces. The viscosity of the "aqueous" phases was adjusted by mixing water with 10, 20, 30vol% glycerol. The continuous lines are fits with Eq.3.1 assuming $R_H=4.0nm$ and $\Theta=90°$. The error bars evaluated from the statistical deviations of the measurements are smaller than the symbol size.*

## 3.4 Small molecular tracers at water-oil interfaces

In this part I investigated the interfacial diffusion of "small" molecular tracers, PDI**1** ($R_H$=1.0nm) and Rhodamine 6G ($R_H$=0.6nm) at interfaces.
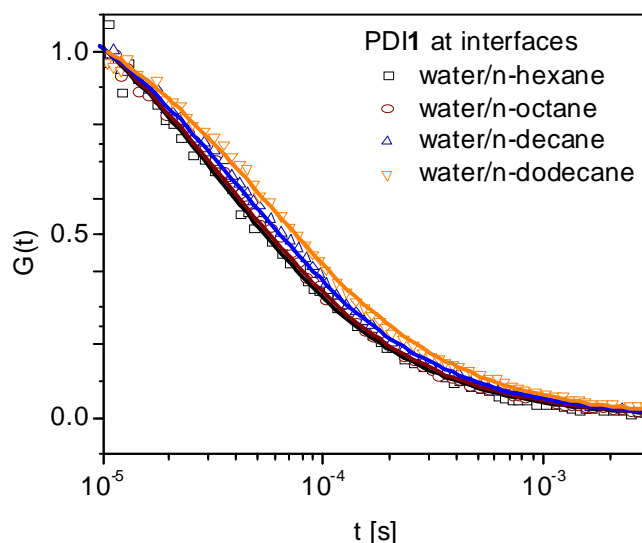


*Figure 3.9* Typical autocorrelation curves and their fits with Eq.2.8 (solid lines) for PDI**1**s

*diffusing at various water/alkane interfaces.*

Typical autocorrelation curves measured for the PDI**1** molecules diffusing at various water-alkane interfaces are shown in Fig. 3.9. The values of the interfacial diffusion coefficients $D_{//}$ obtained for PDI**1** at all studied water/alkane interfaces are plotted vs. the alkane viscosity in Fig.3.10. $D_{\parallel}$ of PDI**1** showed a gradual decrease with the increase of the alkane phase viscosity. This indicates that the PDI molecules penetrate in both phases similar to what was observed for the dendrimer tracers. However, in contrast to the larger dendrimers ($R_H$=4.0nm), the experimentally measured values of $D_{\parallel}$ for the PDI**1** are systematically higher

than the predictions from Eq.3.1 using a hydrodynamic radius of 1.0nm and a contact angle of 90° (Fig. 3.10). Furthermore, these experimental data cannot be represented by Eq.3.1 for any value of the contact angle. Finally and most importantly, at the water-decane interface, where the viscosities of both phases are almost equal, PDI**1** molecules diffuse approximately 1.15 times faster than in bulk water. This indicates that in contrast to the larger dendrimers, the small PDI**1** tracers probe (and are affected by) a molecular scale interfacial layer with a reduced effective viscosity.
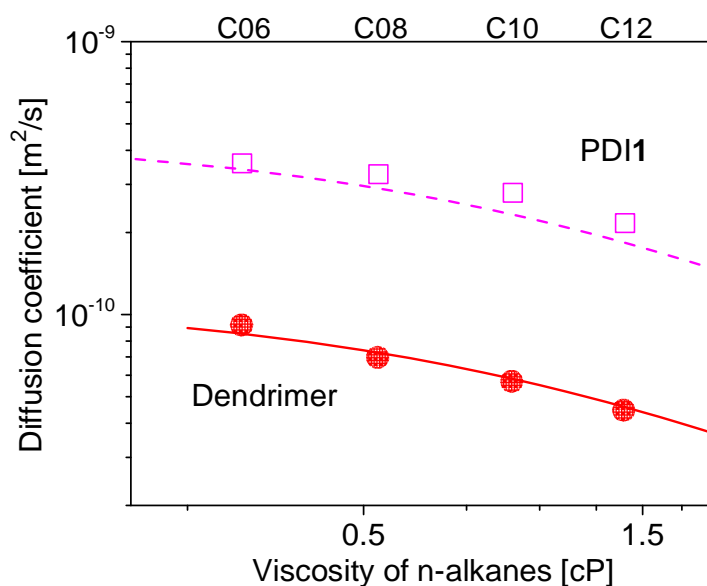


*Figure 3.10. Interfacial diffusion coefficient $D_{//}$ vs. viscosity of the alkane phases measured for the PDI**1** (open squares) and dendrimer (solid circles) molecules at various water-alkane interfaces. The error bars evaluated from the statistical deviations of the measurements are smaller than the symbol size. The dashed and solid continuous lines represent Eq.3.1with $R_H$=1.0 nm for the PDI**1** and $R_H$ =4.0 nm for the dendrimer and $\Theta$=90° in both cases. The Cj on the top of the figure indicates the carbon number of the alkane used.*
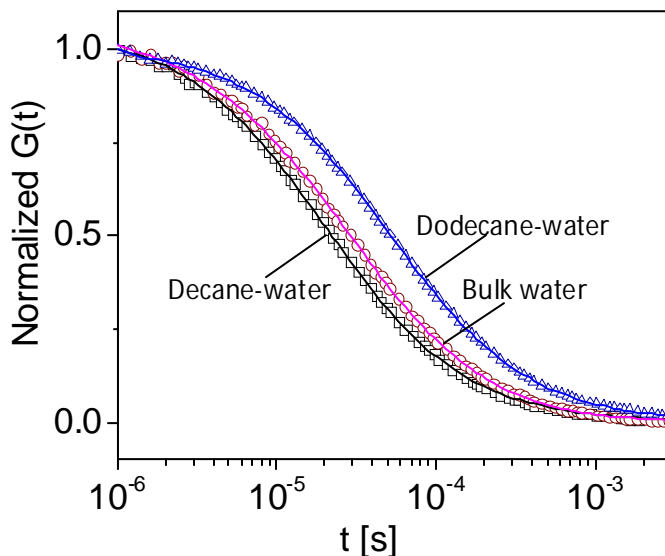
***Figure 3.11*** *Typical autocorrelation curves and their fits with Eq.2.8 (solid lines) for Rhodamine 6G diffusing at water-decane (black squares) and water-dodecane (blue triangles) interfaces. An autocorrelation curve and its fit with Eq.2.5 for Rhodamine 6G diffusing in bulk water (magenta circles) are also shown for comparison.*

The existence of such layer is further confirmed by the diffusion data for the smallest ($R_H$=0.6nm) tracer, Rhodamine 6G. Typical autocorrelation curves measured for Rhodamine 6G diffusing at water-decane and water-dodecane interfaces are shown in Fig. 3.11. For comparison, I also plot an autocorrelation curve of Rhodamine 6G in bulk water. All the experimental curves can be nicely fitted by the two-dimensional or three-dimensional models. The values of the interfacial diffusion coefficients $D_{//}$ obtained for Rhodamine 6G at all studied water-alkane interfaces are plotted vs. the alkane viscosity in Fig.3.12. Compared to

what I have seen about the interfacial diffusion of dendrimers and PDI**1**s, for the smallest tracer the situation is strikingly different.
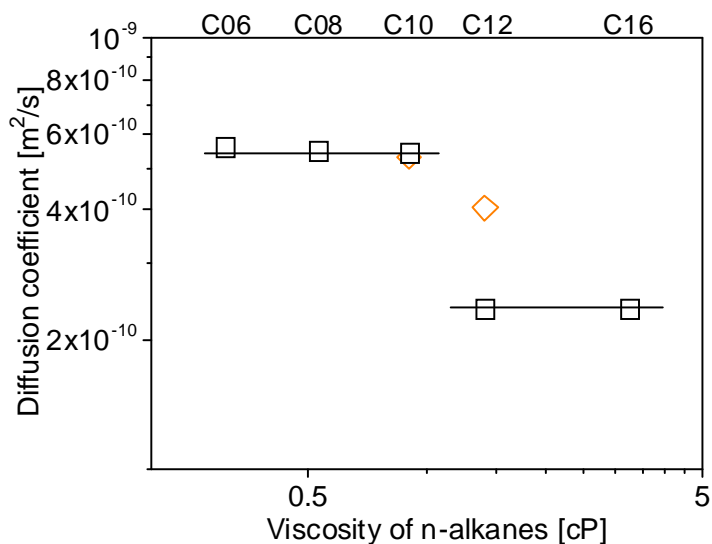


***Figure 3.12*** *Interfacial diffusion coefficient $D_{//}$ vs. viscosity of the alkane phases measured for the Rhodamine  6G at various water-alkane interfaces. The solid line is a guide to the eye for Rhodamine 6G.The Cj on the top of the figure indicates the carbon number of the alkane used. The open diamond symbols represent results for Rhodamine 6G diffusing at interfaces between water and hexane/hexadecane mixtures. The error bars evaluated from the statistical deviations of the measurements are smaller than the symbol size.*

At the water/n-decane interface, the Rhodamine 6G diffuses approximately 1.4 times faster than in bulk water. Moreover, as shown in Fig. 3.12, Rhodamine 6G tracers exhibit a qualitatively different dependence of $D_{//}$ on the n-alkane phases. While the viscosity is changing gradually by one order of magnitude between n-hexane and n-hexadecane, the value of $D_{//}$ is constant ($5.5{\times}10^{-10}$ m$^2$/s) for n-alkanes up to ten carbon atoms. Between n-decane and

n-dodecane the diffusion coefficient decreases to $2.4 \times 10^{-10}$ m$^2$/s. Then it remains constant up to n-hexadecane. Clearly this step-wise behavior cannot be represented by Eq.3.1. In contrast, $D_{//}$ of Rhodamine 6G shows a continuous dependence on the viscosity of the aqueous phases (Fig. 3.13). However, this dependence also cannot be represented be Eq.3.1.
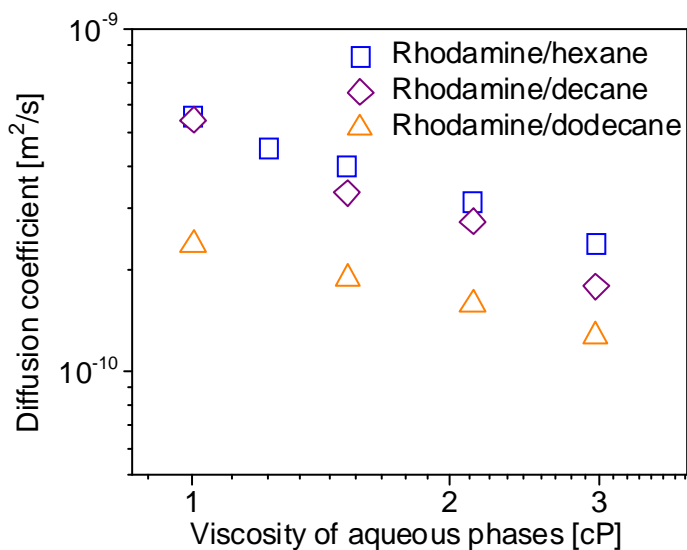


***Figure 2.13*** *Interfacial diffusion coefficient D$_{//}$ vs. viscosity of the aqueous phases for Rhodamine 6G tracers at aqueous/hexane (open squares), aqueous/decane (open diamonds) and aqueous/dodecane (open triangle) interfaces. The viscosity of the "aqueous" phases was adjusted by mixing water with 10, 20, 30vol% glycerol.*

In a different experiment I tuned the viscosity of the alkane phases by mixing hexane with hexadecane at various ratios in order to mimic the viscosities of decane and dodecane. Again, the FCS measurements showed no direct relation between $D_{//}$ of Rhodamine 6G and the alkane phase viscosity (diamond symbols in Fig. 3.12). Indeed, for the hexane/hexadecane

65:35 vol% mixture with a viscosity equal to pure decane, $D_{//}$ is identical to that measured at the water/decane interface. However, for a 48:52 vol% hexane/hexadecane mixture, in which the viscosity is reminiscent of that of dodecane, FCS reveals that $D_{//}$ was higher than that measured at the water/dodecane interface. The increased diffusivity for the 48:52 vol% mixture can be explained by a positive surface excess of hexane since the interfacial tension for water/hexane (49.6 mN/m) is slightly lower than that for water/hexadecane (52.4 mN/m) (Tab.2.1). This confirms that the FCS results on Rhodamine 6G diffusion are highly sensitive to the properties of the water-alkane interface and not directly influenced by the bulk alkane.

As a Rhodamine 6G molecule carry a positive charge, the electrostatic interactions between molecules may also affect their diffusion. Clearly increasing the Rhodamine 6G concentration at the interface should increase the effect of the electrostatic interactions. On the other hand, the electrostatic forces can be screened by adding salts in the solution. FCS experiments provide independent information on the surface coverage at an interface. In a typical measurement, the area per molecule was approximately 0.5 µm$^2$, which was 4-5 orders of magnitude larger than the cross-section of a molecule. Thus, one should not expect any effect from short-ranged interactions. Our control experiment showed that when the area per molecule was 0.003 µm$^2$, $D_{//}$ of Rhodamine 6G at the water-decane interface was approximately 15 % less than the value measured when the area per molecule was 0.5 µm$^2$, i.e. nearly the same. In addition, increasing the tracer's surface coverage may influence the intrinsic property of interfaces. Such effects however were also ruled out by our control experiment. In addition, I tested the effect of salt by measuring the diffusion coefficient of Rhodamine 6G at a water-dodecane interface and adding potassium chloride (with concentration of 10$^{-2}$M) into the water phase. The diffusion coefficient did not change upon

salt addition. This indicates that the electrostatic interactions do not have an effect on the measured interfacial diffusion.

In order to test if surface active contamination influenced the results, in a separate experiment I purposefully added 1 µM sodium dodecylsulfate or Cetyltrimethylammonium bromide to the aqueous phase and measured $D_{//}$ of Rhodamine 6G at a water-decane interface. Neither surfactant resulted in a significant decrease of interfacial diffusion.

## 3.5 Physical model

The experimental results support the following model, as shown in Fig.3.11: At the water-alkane interface there is a reduced viscosity layer. Rhodamine 6G at the interface is continuously located towards the aqueous phase while PDI**1**s and dendrimers span across the interface. A different but in both cases significant fraction of the cross-section of each Rhodamine 6G and PDI**1** molecule is located within this high mobility and high entropy region. As a result they experience different degrees of the reduced effective viscosity and diffuse faster than in bulk. A reason for the existence of this high mobility region could be the presence of dangling OH bonds at the water-alkane interface [4, 5]. This picture is supported by recent non-linear spectroscopy studies that found ultrafast reorientational motion of water molecules at air/water interface [100-103]. The larger dendrimer tracers with a hydrodynamic radius of 4.0 nm are symmetrically immersed in both the aqueous and the alkane phases. Their size is much larger than the 2 to 4 Å correlation length in bulk water [104, 105] that provides the natural length scale over which structural anomalies at interfaces tend to decay

[106-108]. As a consequence, their diffusion could be adequately represented by surrounding viscosity.
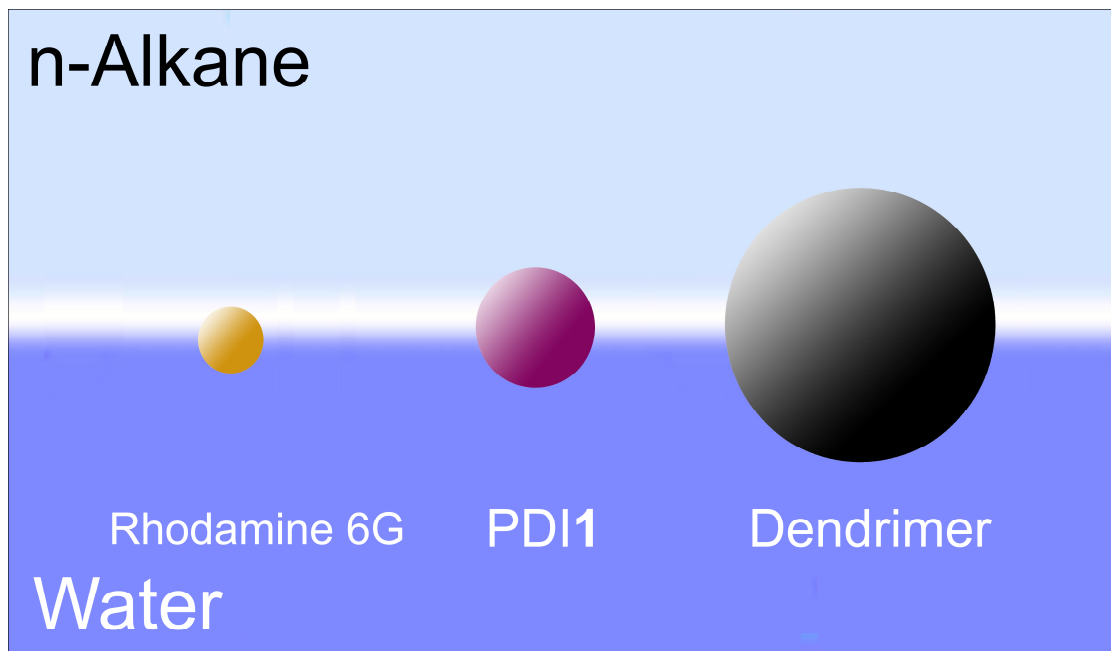


*Figure 3.11 Schematic presentation of the physical model. The Rhodamine 6G (the yellow sphere), PDI1 (the pink sphere) and dendrimer (the black sphere) are suspended at an interface between immiscible liquids, water (purple) and alkane (bright blue). The white bar at an interface indicates the reduced viscosity layer. Parts of Rhodamine 6G molecules are dissolved in waterside while a fraction of Rhodamine 6G molecules is located at this reduced viscosity region. For the PDI1 and dendrimer molecules, both of them span across the WO interface.*

This model explains our experimental observations for PDI**1** and dendrimer diffusion at all studied water-alkane interfaces and the Rhodamine 6G diffusion at the water-hexane, water-octane, and water-decane interfaces. However, for Rhodamine 6G diffusing at the

longer alkanes-water interfaces, i.e. dodecane and hexadecane the situation is more complex. As shown in Fig. 3.12, for these alkanes $D_{//}$ of Rhodamine 6G decreases stepwise to a value of $2.4\times10^{-10}$ m$^2$/s. This is even lower than the diffusion coefficient in bulk water ($3.82\times10^{-10}$ m$^2$/s at 22°C).

In the following I discuss the relevant length-scales that appear at the WO interface, relating them to phenomena that can explain the stepwise slow-down of interfacial diffusion. For the water-alkane interfaces, the capillary wave may influence the interfacial diffusion of tracer molecules. The capillary wave theory predicts the interfacial width of water-alkane by [109]

$$\sigma^2 = \frac{1}{4} B \ln[(q_u^2 + \kappa^2)/\kappa^2] \tag{3.2}$$

Here, $\sigma^2$ is the total intrinsic mean-square surface displacement; $B = k_B T/\pi\gamma$ is a parameter where $k_B$ is the Boltzmann constant, $T$ is the temperature, $\gamma$ is the interfacial tension at $T$; the upper cutoff $q_u = 1\text{Å}^{-1}$ as provided by the typical molecular length scale $2\pi/q_u$, the gravitational cutoff $\kappa^2 = \Delta\rho g/\gamma$, where $\Delta\rho$ is the difference in mass density across the interface; $g$ is the gravitational acceleration. Then, the total intrinsic mean-square surface displacement $\sigma$ of water/alkane is 6.8 Å, which is very close to 7 Å. However this value is almost identical for all investigated systems and therefore cannot explain the observed stepwise slow-down. In water, the relevant length scale that leads to a disruption of the hydrogen bond network is provided by the crossover from volume to surface scaling in the solvation free energy for hydrophobic cavities. This value of approximately 10 Å is indicative for the curvature of an interface that allows elastic rearrangement of the water molecules, thus distorting rather than

breaking their hydrogen-bonding network[1]. However, this transition happens gradually and therefore is unlikely to cause the sudden change observed by FCS.

The next important scale in the problem is given by the size of the Rhodamine 6G molecule i.e. $R_H = 0.6$ nm or its physical radius that is around 0.36 nm along the conjugation segment (Fig.2.5). For alkanes, the radius of gyration provides the characteristic length scale that governs interfacial properties such as the intrinsic width [28]. The diffusion slow-down happens between decane and dodecane that have radii of gyration of 3.0 and 3.5 Å, respectively. Considering these length scales indicates that the stepwise decrease of $D_{//}$ coincides with alkane coil size that matches the size of Rhodamine 6G. This finding is also consistent with earlier fluorescence recovery after photobleaching studies by Kovaleski and Wirth[110], which indicated that not the viscosity of alkanes, but rather the interfacial roughness is slowing down the lateral diffusion at long chain alkane-water interfaces. Such assumption can explain our results, supposing that the decrease in diffusion coefficient (as compared to the bulk water value) on the water-dodecane and water-hexadecane interfaces is overcompensated from a slowdown resulting from e.g. the interfacial roughness. Finally, it should be mentioned that in contrast to the Rhodamine 6G, the PDI**1** molecules were not directly affected by the interfacial roughness and did not show a step wise change in $D_{//}$ with alkane viscosity. This is related to the fact that the larger and more amphiphilic PDI molecules penetrate in both phases, i.e. spans across the interface and thus their diffusion is not directly influenced by the gyration radii of alkanes.

In summary, I reported a new strategy to study the controversial question of the existence and the properties of interfacial water adjacent to a hydrophobic surface. Rather

than measuring structural and spectroscopic properties I directly probed the interfacial dynamics via the diffusion coefficient of single molecular tracers as a function of viscosity of both liquid phases and the tracer's size. My results indicate the existence of an interfacial region with reduced effective viscosity and increased mobility that decays over a length scale on the order of a water monolayer towards bulk dynamics.

# CHAPTER 4

## Nanoparticle Diffusion at water-oil interfaces

In this chapter, I performed an exploitation to study the diffusion of fluorescent semiconductor NPs at planar water-oil interfaces using FCS. The effects of several important parameters, i.e. the particles size, the surface chemistry (hydrophobic/hydrophilic), the asymmetric feature, and the oil/aqueous phase viscosity were investigated. Because of the high tendency of NP to aggregate at WO interfaces, FCS is well suited as it offers the possibility to monitor the diffusion at WO interfaces even for very small NP with high mobility and at very low surface coverage [95, 111].

In the first part of this chapter, the interfacial diffusion of symmetric NPs with different surface properties and with various sizes was investigated. A noticeable decrease in $D_\parallel$ as compared to what can be expected from the surrounding bulk viscosities was observed. Afterwards, I ran a comparative study to investigate the interfacial diffusion of spherical NPs with Janus motif at WO interfaces. The so-called Janus NPs, immiscible in both liquid phases, exhibited a significant decrease in $D_\parallel$ as compared to that of their symmetric counterparts.

## 4.1 Interfacial diffusion of Symmetric nanoparticles at water-oil interfaces

### 4.1.1 Nanoparticle diffusion in bulk

The interfacial mobility of four different types of symmetric quantum dots (QDs) with various sizes and surface functionalities was studied (Table 4.1). The hydrophilic quantum dots were coated with carboxyl-derivatized amphiphilic polymers that make them easily dispersible in water. In the text below these hydrophilic, water soluble NPs are referred to as $QD_{w-j}$ where $j$ indicates their hydrodynamic radius ($R_H$). For comparison the hydrophobic quantum dots $QD_{o-j}$ that are coated with aliphatic hydrocarbons were also studied. Fig.4.1 shows typical autocorrelation curves for QD diffusing in either bulk water or bulk decane. The experimental curves could be adequately represented by Eq.2.5, yielding the diffusion coefficient. The hydrodynamic radii then can be calculated by Stokes-Einstein equation, as illustrated in Tab. 4.1.

***Table 4.1*** *hydrodynamic radius of the samples measured by FCS*

| Particle | $R_H$ (nm) | Surface property |
|:---:|:---:|:---:|
| $QD_{W-5}$ | 5.9 | hydrophilic |
| $QD_{W-8}$ | 8.7 | hydrophilic |
| $QD_{W-11}$ | 11.1 | hydrophilic |
| $QD_{O-5}$ | 5.0 | hydrophobic |
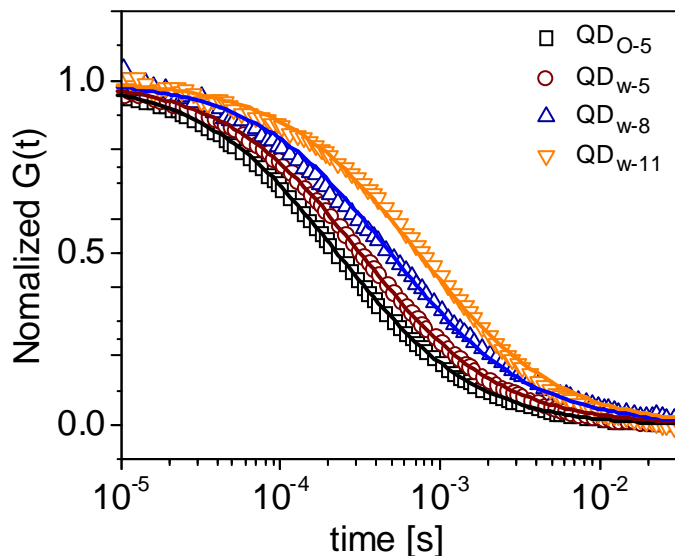
**Figure 4.1** *Normalized autocorrelation curves of QD$_{O-5}$ in bulk decane and QD$_{w-j}$s in bulk water.*

**4.1.2 Procedure to form the WO interfaces suspended with NPs**

$D_{//}$ of the QDs at the water-alkane interfaces (D$_\parallel$) were measured by FCS. A laser beam was tightly focused by a high numerical aperture microscope objective. The excited fluorescence was collected by the same objective and directed to an avalanche photo diode detector (APD). By shifting the objective in vertical direction the position of the focus can be scanned through the sample with 200 nm for each step. A typical scan through the water-hexane interface, at which QD$_{w-5}$ are deposited is shown in Fig. 4.2a. The fluorescence signals are detected only when the focus is proximity to the WO interfaces. This confirms that the QDs reside at the interface only. Fig. 4.2b and c shows the fluorescence fluctuation and the corresponding autocorrelation curve when the focus is precisely adjusted in the intensity maximum. It is seen that the experimental curve can be adequately fitted by Eq.2.8. It is well

known that QDs with a hydrophobic shell tend to absorb at interfaces due to minimum of the free energy[50]. For the charged NP, one could expect that the acidic groups on the surfaces of NPs show a lower dissociation in the oil phase compared to that in the water side [112]. The charge reduction of a NP creates an energy barrier for its penetration into oil phase. However, Fig.4.2a and a number of previous studies [63, 113, 114] showed that the charged NPs can also be stabilized at water-oil interfaces. This could be interpreted as merely parts of carboxylates on the NP surface are ionized due to the electrostatic repulsions between neighboring charged-groups at the same NP. As a result, the charge may not change a lot when a NP modestly pierces into the oil phase. [115].
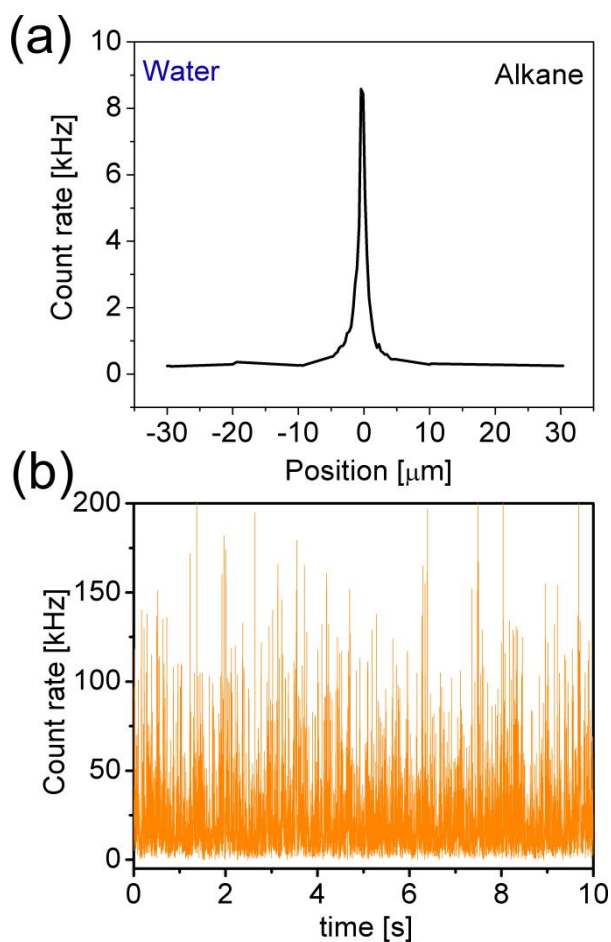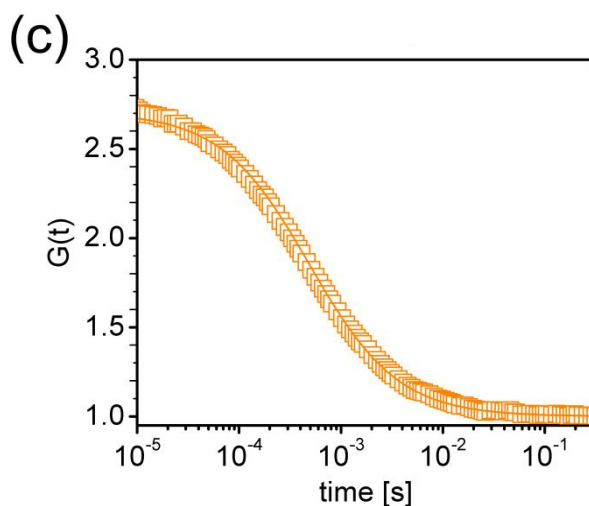
*Figure 4.2: (a) A Fluorescence intensity scanning through a water-hexane interface suspended with QD$_{W-5}$. The scanning is done by moving the focus from water phase to alkane phase with a step of 200nm. (b) Representative fluorescence fluctuations versus time at the intensity peak. (c) The corresponding autocorrelation function of the QD$_{w-5}$ (open square) diffusing at a hexane-water interface, which can be adequately fitted by Eq. 2.8(solid line).*

### 4.1.3 Hydrophobic nanoparticle diffusion at water-oil interfaces

Fig. 4.3 shows typical normalized FCS autocorrelation curves for QD$_{o-5}$ diffusing at water-alkane interfaces. The experimental autocorrelation curves are adequately represented by Eq.2.8. The average diffusion time through the FCS observation volume increased as increasing the viscosity of the alkanes ($\eta_a$). This is further illustrated in Fig 4.4, where the diffusion coefficient of QD$_{o-5}$ at water-alkane interfaces, $D_\parallel$, is plotted vs. the viscosity. For comparison, the diffusion coefficient of the same quantum dots measured in bulk alkanes, $D_{bulk}$, is also plotted. The later decreases as $D_{bulk} \sim \eta_a^{-\alpha}$ with $\alpha \approx 1$ as expected for free 3D

Brownian diffusion. At the water-alkane interfaces the diffusion coefficient decreases less steeply, i.e. $D_\parallel \sim \eta_a^{-\alpha}$ with $\alpha = 0.44$. This can be attributed to the fact that the QDs are only partially immersed in the alkane phase and thus only partially affected by its viscosity[116].
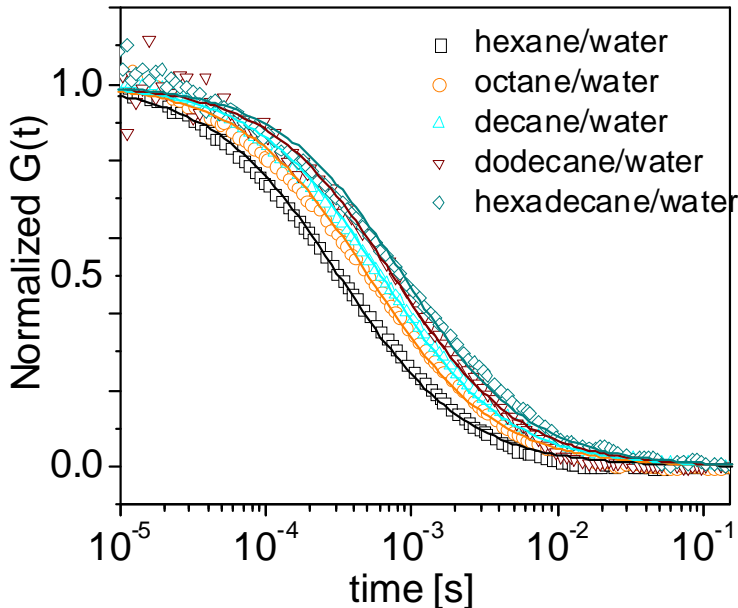


***Figure 4.3****: Normalized experimental autocorrelation curves of $QD_{o-5}$ at different water-alkane interfaces (symbols) and the corresponding fits with eq. 2 (solid lines).*

$D_\parallel$ is lower than $D_{\text{bulk}}$ in most of the cases, which implies that the QDs diffuse more slowly when they are at interfaces. This finding cannot be explained merely by viscosity differences between water and alkanes. Indeed the viscosity of the water is higher than that of the alkanes and may lead to a diffusion slowdown only in the case of the short alkanes, e.g. hexane and octane (the first 2 points in Fig. 4.4). The longer alkanes have higher viscosities than water and thus the partial immersion of the NPs in the water phase should lead to an

increase of the diffusion coefficient, which was not observed. For the water-decane interface the viscosities of both liquids are similar. Nevertheless the diffusion coefficient at this interface is approximately two times smaller than in bulk decane. This effect cannot be explained with classical theories [117].
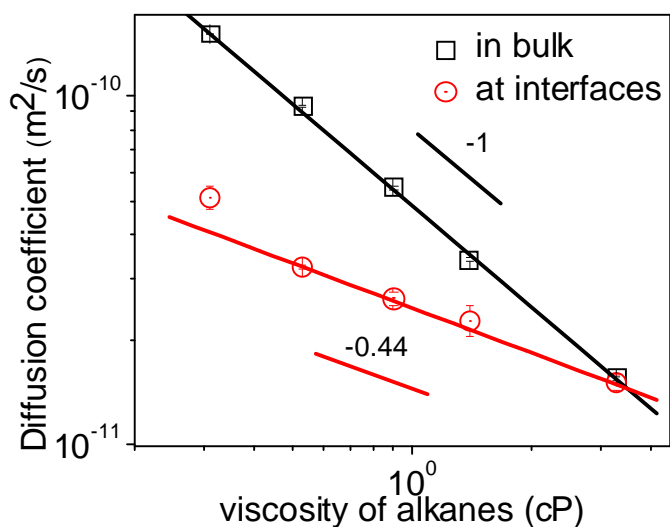


***Figure 4.4***. *Diffusion coefficient of $QD_{o-5}$ diffusing in bulk and at the corresponding water-alkane interfaces versus viscosity of alkanes.*

## 4.1.4 Hydrophilic nanoparticle diffusion at water-oil interfaces

The diffusion of charged NPs trapped at the water-oil interface can be affected by long-ranged electrostatic interactions [112, 118-120]. As the overall charge of $QD_{o-5}$ is not well known and probably small, I proceeded by studying the interfacial diffusion of water dispersible carboxylated QDs that carry a negative charge. Typical examples of experimental autocorrelation curves measured for these QDs that also easily adsorbed at water-alkane

interfaces are shown in Fig.4.5. The autocorrelation curves can be adequately fitted by Eq. 2.8 yielding the corresponding interfacial diffusion coefficient, $D_\parallel$. Fig. 4.6a shows $D_\parallel$ versus viscosity of alkanes for $QD_{o-5}$ and several carboxylated water soluble quantum dots with different sizes, $QD_{W-j}$. The charged $QD_{W-5}$ diffuses faster than the weakly (non) charged $QD_{o-5}$ in spite of their similar sizes. This indicates that electrostatic interactions are not the reason for the slowdown of interfacial diffusion. This was further confirmed by control experiments, showing that $D_\parallel$ of $QD_{W-11}$ at an octane-water interface did not change upon adding a salt (potassium chloride) with concentration of $10^{-2}$-$10^{-3}$M to the water phase.
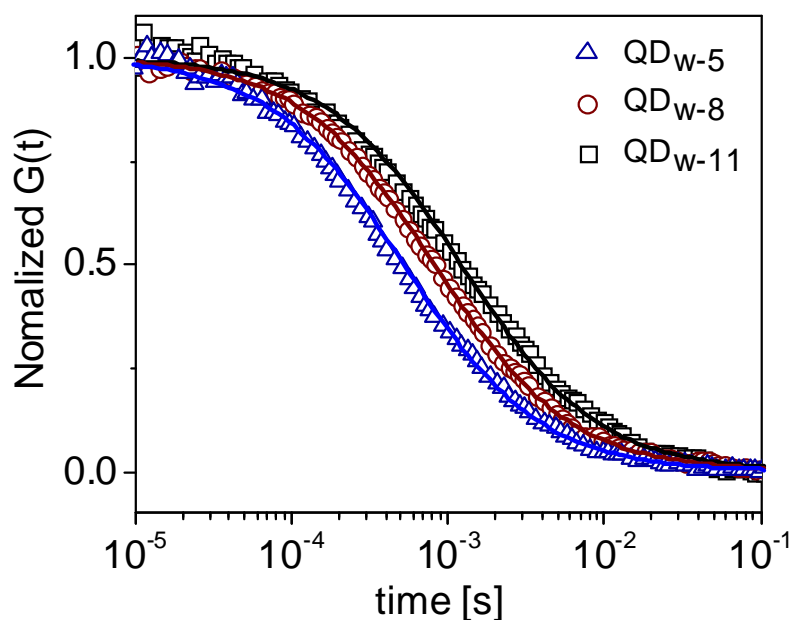


***Figure 4.5*** *Normalized autocorrelation curves of $QD_{W-j}$ at water-decane interfaces. Each of them can be adequately fitted by Eq. 2.8 (solid line).*

The double logarithmic plots (Fig. 4.6) show that the dependence of the interfacial diffusion coefficient on the radius of the QD and on the viscosity of alkanes can be described by a power laws according to

$$D_{\parallel} = a\eta_a^{-\alpha} R_H^{-\beta} \tag{4.1}$$

Here, $\alpha$ and $\beta$ are empirical constants. Their values obtained by the fits to the experimental data (Fig.4.6) are tabulated in Tab.4.2. Two conclusions can be drawn: (1) $\alpha$ slightly decreases with increasing $R_H$; (2) $\beta$ increases from hexane-water to hexadecane-water interfaces.

*Table 2 $\alpha/\beta$ deduced from equation 2.*

| Alkanes | QD$_{w5}$ | QD$_{w8}$ | QD$_{w11}$ |
|---|---|---|---|
| hexane | 0.35/0.89 | 0.51/0.89 | 0.53/0.89 |
| octane | 0.35/1.19 | 0.51/ 1.19 | 0.53/1.19 |
| decane | 0.35/1.29 | 0.51/ 1.29 | 0.53/1.29 |
| Dodecane | 0.35/1.39 | 0.51/ 1.39 | 0.53/1.39 |
| Hexadecane | 0.35/1.37 | 0.51/ 1.37 | 0.53/1.37 |
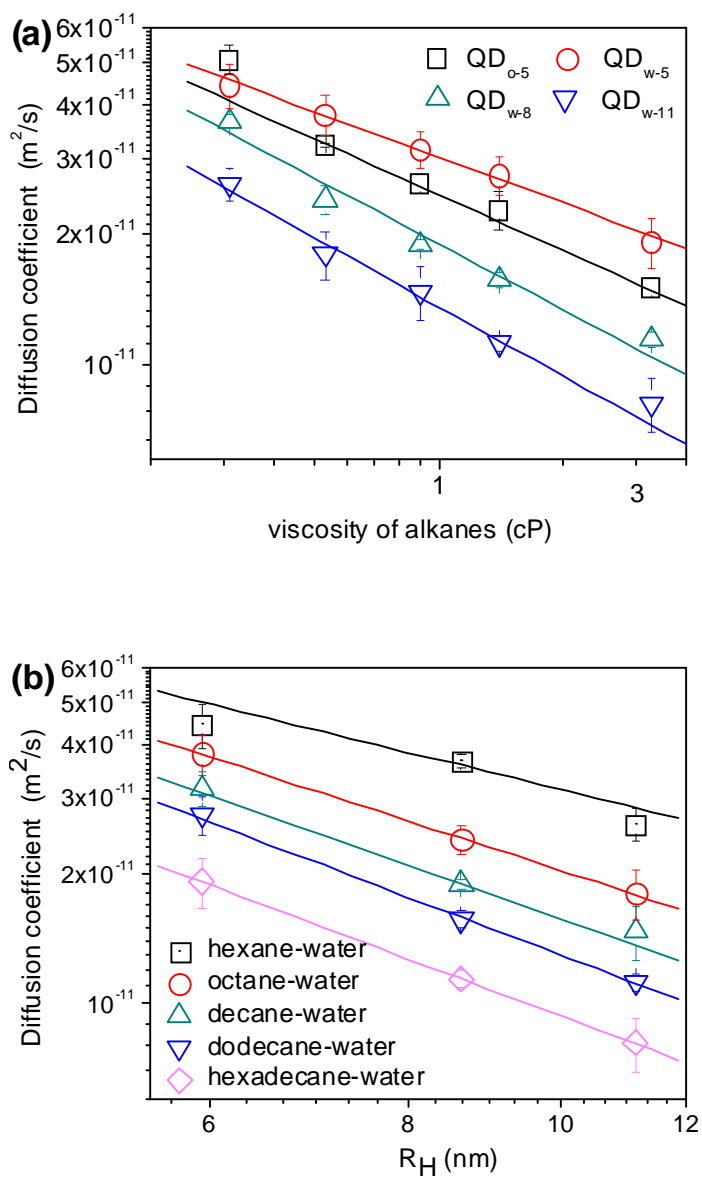
**Figure 4.6** *Diffusion coefficients $D_{||}$ of $QD_{W-j}$ at the water-alkane interface as a function of (a) viscosity of alkanes and (b) hydrodynamic radius of particles.*

**4.1.4 Possible artifacts for the slowdown**

Before further interpretation, it is important to consider (and exclude) some possible artifacts that may lead to an apparent slowdown of interfacial diffusion. For example, a high surface coverage could induce cluster formation thus influencing (decreasing) the interfacial diffusion. In extreme cases, the particles may self-assemble in a monolayer at the WO interfaces[65]. Russell and coworkers have used fluorescence photobleaching techniques to measure the NPs mobility in such monolayers and found that the in-plane diffusion coefficient of NPs is 4 orders of magnitude lower than the diffusion coefficient of the same NPs dispersed in toluene, as measured by dynamic light scattering [76]. In addition, the interfacial diffusion of NPs is concentration dependent [77]. The reduction of $D_\parallel$ can be attributed to the confined effect to which a crowd of NPs limits the free diffusion of individual NPs [77] and to the increased possibility of particle-particle interactions[121]. These pioneering works motivated me to extract the diffusion of single NPs at water-oil interfaces. To exclude this effect mentioned above, I have prepared samples with a particularly low surface coverage. Furthermore the fits to the FCS autocorrelation curves (e.g., Fig.4.1c) provide independent information for the average number of particles in the observation volume and thus for the particle concentration at the interface. Using these fits I estimated that the area per QD in the experiments was approximately 0.2-0.5 $\mu m^2$, which is three or four orders of magnitude larger than the cross-section of the NPs. Thus, one should not expect any effect from short-ranged particle-particle interactions. Furthermore the presence of NP clusters (aggregates) should be also excluded as such clusters are easily detected in a FCS experiment by their anomalously high brightness as compared to the individual NPs. In order to get better insight on this effect I have prepared several water-

alkane interfaces with different concentrations of the dispersed QDs and measured the NP interfacial diffusion. The corresponding FCS autocorrelation curves (Fig. 4.7) show that until certain threshold, the NP concentration (surface coverage) does not affect the interfacial diffusion. An increase of concentration associated with increased brightness of detected single chromophores, however, leads to cluster formation and much slower interfacial diffusion.
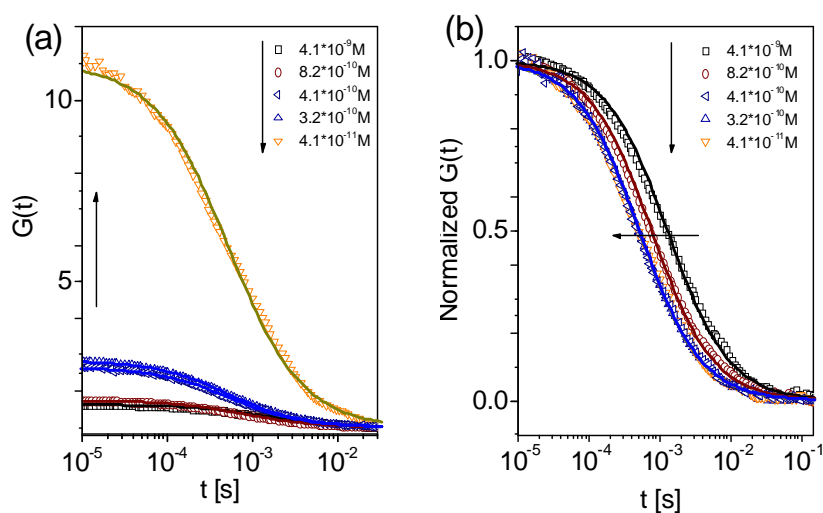


***Figure 4.7*** *(a) Autocorrelation curves measured for $QD_{w-5}$ diffusing at the water-decane interface at different surface coverages. The symbols correspond to different QD concentrations in the water phase before adding the decane phase. The arrows indicate the direction of decreasing the QD concentration (surface coverage). The decrease of G(0) that is reversely proportional to the number of particles in the observation volume (Eq.2.8) clearly confirms the increase of the surface coverages; (b) The same data as (a) but normalized to the same value of G(0) for better comparison of the corresponding diffusion times (decay times). Clearly the diffusion time does not change with QD concentration until certain threshold value of about $4*10^{-10}M$. At higher concentrations the diffusion is slowed down significantly.*

Another possible reason for the slowdown of the QDs at the water-alkane interface may be the presence of some unknown solutes possessing a strong surface activity and consequently enriching at the interface[89]. Based on an intuitive understanding, this may hinder the movement of the QDs by increasing the drag force that they experience and therefore result in a decrease of the diffusion coefficient of QDs at the interface. To avoid such effects I took a special care in cleaning the sample cells and the corresponding liquids. Furthermore I have measured the interfacial tension for all water-alkane interfaces by the Du-Noüy ring tensiometer as tabulated in Tab.2.1. The obtained values agree with those reported in the literature within the statistical error, confirming the purity of the WO interfaces studied. Finally I explored in a controlled way how the presence of surfactants influences the interfacial diffusion of the QDs. For that purpose, I added sodium dodecylsulfate with a concentration of $10^{-4}$M into the aqueous phase before the deposition of $QD_{w-5}$ and creation of a water-decane interface. This resulted in a continuous increase of $D_{\parallel}$ over approximately 1 hour (reflecting the adsorption of the surfactant molecules on the interface) to a final value much higher than that measured when pure water was used as the aqueous phase. In contrast, $D_{\parallel}$ showed no time dependence in the absence of surfactant. Thus, I conclude that the observed slowdown of the QDs at the interface is not affected by adsorption of impurities at the interface.

## 4.2 Interfacial diffusion of Janus NPs at WO interfaces

Janus NPs [122], in which the surface of a particle is divided into several areas with different chemical properties, attracted considerable attention because of their extremely high interfacial activity. Compared to their symmetric counterparts, placing them at WO interfaces

could effectively decrease the interfacial tension. Little is known about what happens for single Janus NPs at WO interfaces. To explore this issue, I initialize the following study. I used FCS [95] to study the lateral diffusion of Janus and symmetric NPs at water/n-alkane interfaces and explore the underlying mechanism of the interfacial diffusion of NPs at WO interfaces.

**4.2.1 Janus nanoparticle diffusion in bulk**

Herein, I used the spherical Janus NPs functionalized with one hemisphere of polyethylene glycol and the other hemisphere of twelve carbon alkane [123, 124]. A symmetric NP functionalized with polyethylene glycol only which also could be absorbed at water-oil interfaces[125, 126], was used for comparison. Both types of NPs were dissolved in dichloromethane. A typical TEM picture is shown in Fig.4.10c, indicating that the Janus NPs used here is spherical. Fig.4.9 shows typical autocorrelation curves for QD diffusing in bulk dichloromethane. The experimental curves could be nicely represented by Eq.2.5, yielding the diffusion coefficient. The hydrodynamic radius then can be calculated by Stokes-Einstein equation, yielding $R_H$ =5.0 and 6.4 nm for Janus and symmetric NPs, respectively.
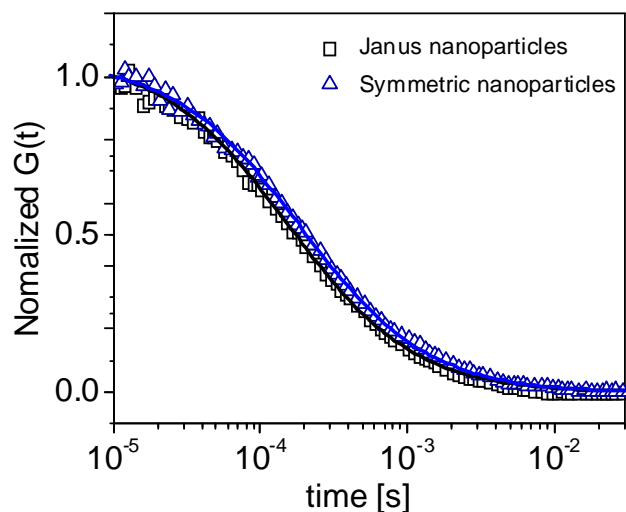
*Figure 4.9* *Normalized autocorrelation curves of Janus and symmetric NPs in bulk*

*dichloromethane.*

**4.1.2 Procedure to form the water-oil interfaces suspended with Janus nanoparticles**

The Janus NPs used in this thesis are only dissolved in dichloromethane. Thus, the symmetric NPs are also dissolved in dichloromethane for comparison. To prepare water/n-alkane interfaces suspended with Janus NPs, first, the sample cell, an Attofluor chamber (Molecular Probes, USA) with a microscope cover slip bottom, was filled to a height of $\approx 100$ µm with aqueous solution. Then a drop of $\approx 4$ µL dichloromethane solution of NPs with a concentration of roughly $10^{-10}$M was added. After the dichloromethane solutions are totally evaporated, the n-alkanes were gently added on top of the aqueous phase. Because self-assembly of Janus NPs is ubiquitous in bulk phases or at interfaces [127-129], the surface coverage should be low enough to eliminate the interparticle interaction and minimize the possibility of particle contact [112, 118, 121, 130]. Therefore, in a typical FCS measurement,

the surface coverage of non-charge Janus NPs was commonly below 1-2 $\mu m^2$ per particle. Fluorescence fluctuations from viable clusters were distinguished from its ultra-high fluorescence and therefore could be excluded.

NPs were excited by the 488 nm line of an Argon laser focused in the middle of a WO interface (Fig. 4.10a) by a water immersion microscope objective (C-Apochromat 40×, NA 1.2, Carl Zeiss, Germany). The fluorescence was collected by the same objective, and finally directed to an avalanche photodiode detector by passing a confocal pinhole and emission filter. No fluorescence could be monitored if the focus was moved away from the interface (Fig. 4.10b).

Fig. 4.10d illustrates typical autocorrelation curves measured for interfacial diffusion of Janus and symmetric NPs at a water-decane interface. The experimental data can be nicely represented by Eq.2.8, indicating a two-dimensional diffusion. The single decay found for NPs at WO interfaces indicates that the diffusion detected is originating from rather monodisperse species. Fig.4.10d illustrates a large increase in the decay time for Janus NPs.
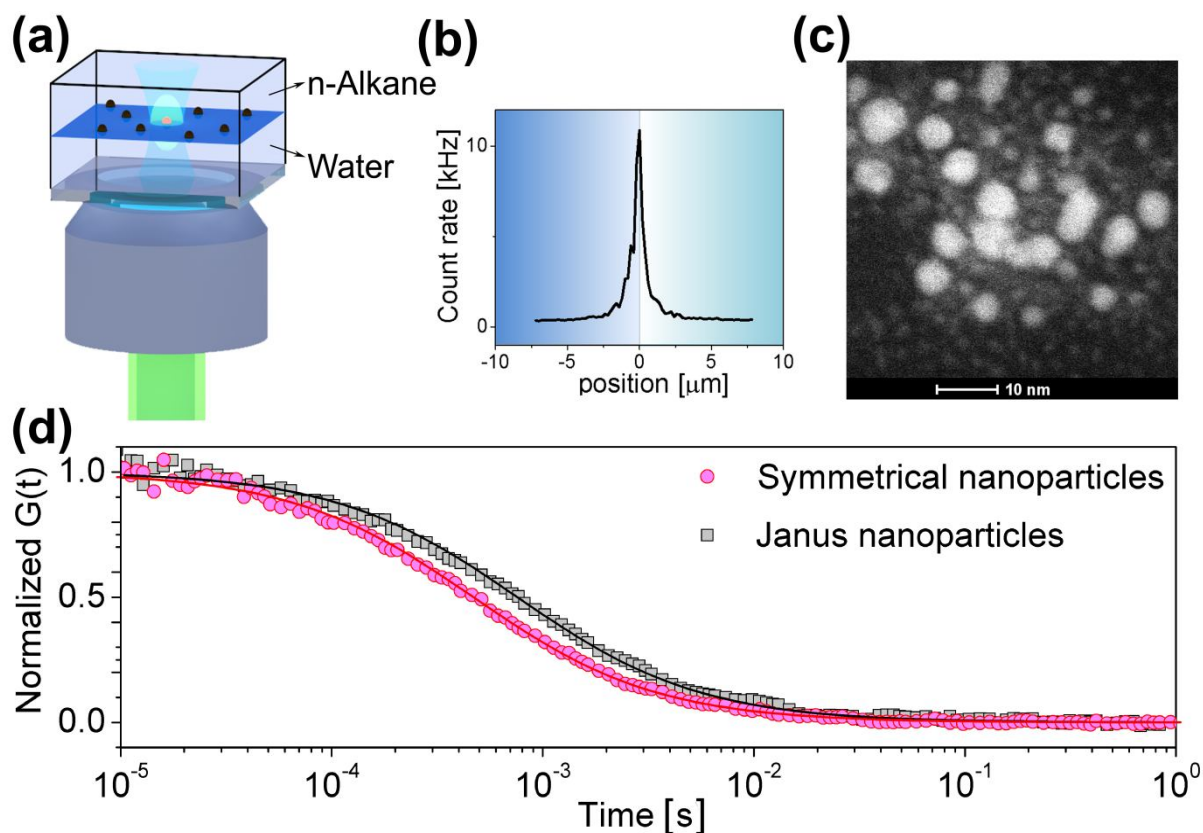
***Figure 4.10*** *(a) A Scheme of the focused laser beam at the middle of a WO interface; (b) A fluorescence intensity scanning through a water/n-decane interface suspended with Janus NPs. The scanning is done by moving the focus from water phase to decane phase with steps of 200 nm; (c) A typical transmission electron microscope (TEM) picture of Janus NPs: both polyethylene glycol and n-alkane chains are expected to be invisible in TEM; (d) Typical autocorrelation curves and their fits with Eq.2.5 (solid lines) for Janus and symmetric NPs diffusing at a water-decane interface.*
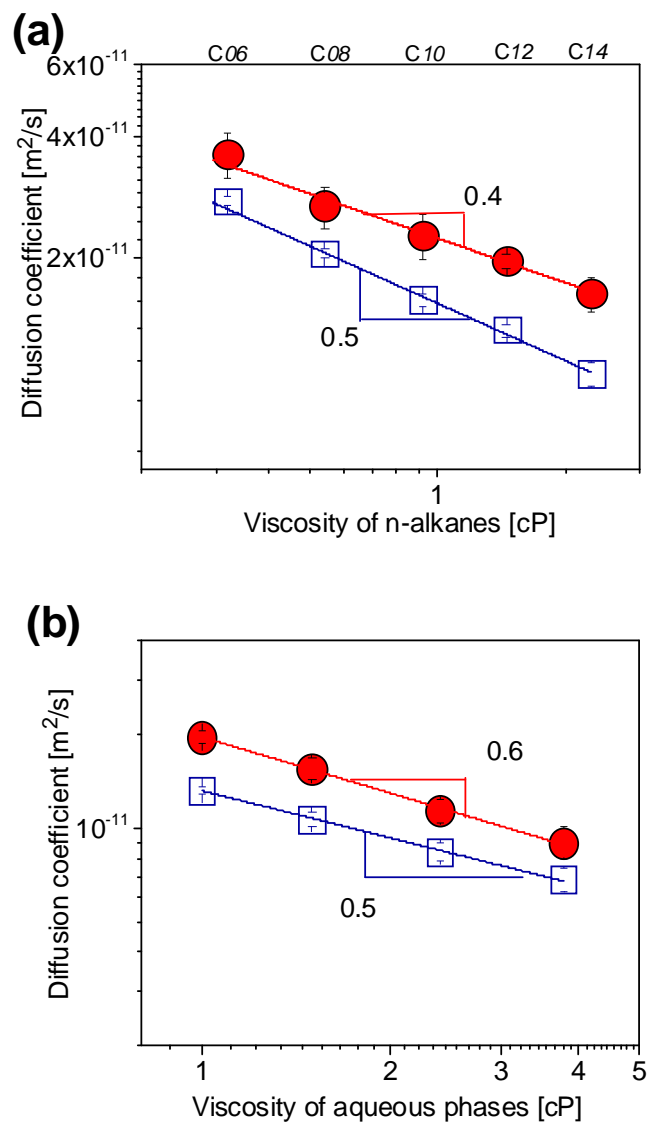
**Figure 4.11** *(a) Interfacial diffusion coefficient D<sub>//</sub> vs. viscosity of the alkane phases for Janus (open blue squares) and symmetric (solid red circles) NPs diffusing at various water-alkane interfaces. The Cj on the top of the figure indicates the carbon number of the n-alkane used; (b) D<sub>//</sub> vs. viscosity of the aqueous phases for Janus (orange squares) and symmetric (red circles) NPs at aqueous-dodecane interfaces. The viscosity of the "aqueous" phases was adjusted by mixing water with 10, 23, 34vol% glycerol. The error bars were evaluated from the statistical deviations of the measurements.*

90

### 4.1.3 Effect of surrounding viscosity

The values of the interfacial diffusion coefficients $D_{//}$ obtained for both NPs are plotted against the viscosity of both alkane and aqueous phases, as shown in Fig. 4.11. The viscosity of the aqueous phases is tailored by adding different amounts of glycerol.

For symmetric particles a gradual decrease of $D_{//}$ with the increase of alkane viscosity $\eta_a$ was observed (red circles in Fig. 4.11). By fitting the experimental data with a scaling law $D_{//} \sim \eta_a^{-\alpha}\eta_w^{-\beta}$ the following parameters were obtained $\alpha = 0.4$ and $\beta = 0.6$. This must be attributed to the fact that symmetric particles are partially immersed in each phase and thus only partially affected by its viscosity. In the particular case of a water-decane interface, where viscosities of the two phases are similar, $D_{//}$ is slower as compared to a value calculated according to Eq.3.1. This is in good agreement with previous experimental and numerical studies [111, 131-135].

A key feature is that the interfacial diffusion of Janus NPs is strikingly slower than that of symmetric particles at all interfaces studied. In double logarithmic plots, the dependence of $D_{//}$ on the viscosity of both n-alkane and aqueous phases in log-log plots yields $\alpha = \beta = 0.5$, demonstrating an almost equal contribution of viscosities from both liquid sides (Fig.4.11). This is in good agreement with previous theoretical calculation[136]. As a comparison, $\alpha = 0.4$, $\beta = 0.6$ for symmetric NPs at interfaces may qualitatively suggest that these NPs (symmetric) locate toward waterside of the WO interfaces. Remarkably, the interfacial diffusion behavior is in good agreement with what one has observed for $QD_{W-5}$, leading to a consistent picture of the hydrophilic NPs at WO interfaces.

## 4.1.4 Effect of interfacial tension

In different experiments, I compared the diffusion of Janus NPs at water-octane and water-toluene interfaces, as illustrated in Fig. 4.12. The interfacial tension of the water/toluene interface ($36mN^{-1}$ m) is modestly lower than that of the water-octane interface ($51$ $mN^{-1}$ m) but the viscosities of octane and toluene are similar. If one assumes that the wettability of Janus NPs at both interfaces is the same, this experimental results (Fig.4.12) indicate that the interfacial tension also influence the NP interfacial diffusion.
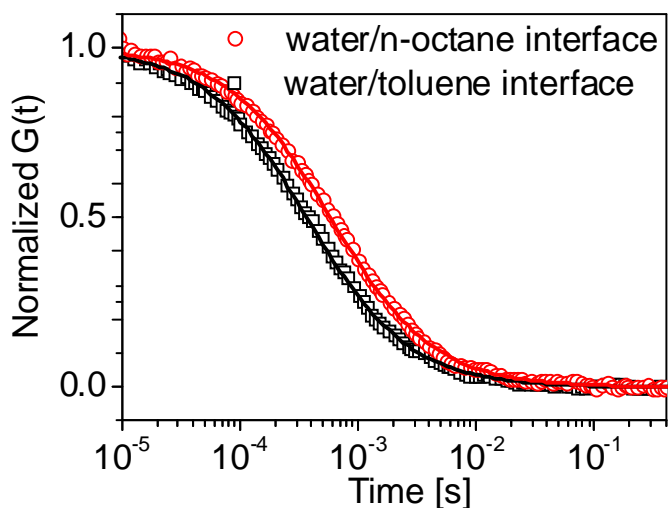


*Figure 4*.12 *Typical autocorrelation curves and their fits with Eq.2.8 (solid lines) for Janus NPs diffusing at water-toluene (black squares) and water-octane (red circles) interfaces.*

It is instructive to calculate the desorption energy of NPs at WO interfaces. The energy needed to remove a Janus particle from an interface to one of the liquid phase can be calculated by macroscopic theories in terms of the three phase contact angle. For the global

contact angle $\beta \geq \alpha$ (represents the relative ratio of the polar and apolar areas), the energy is expressed by [67]

$$E(\beta) = 2\pi R_H^2 [\gamma_{AO}(1 + \cos\alpha) + \gamma_{PO}(\cos\beta - \cos\alpha) + \gamma_{PW}(1 - \cos\beta) - 0.5\gamma_{AO}(\sin^2\beta)] \quad (4.2)$$

Here, $\gamma_{AO}$, $\gamma_{PO}$ and $\gamma_{PW}$ correspond to the interfacial tension of the WO interface, oil-polar region of particles and water-polar region of particles, respectively. The average contact angle $\theta_{aver}$ can be calculated by $(\theta_p(1+\cos\alpha) + \theta_a(1-\cos\alpha))/2$. The three-phase contact angles $\theta_p$ and $\theta_a$, represent the three-phase contact angles for homogeneous particles with surface properties equal to the hydrophilic or hydrophobic regions of the Janus NPs. For the Janus NPs used, the values of $\theta_p$ and $\theta_a$ are 98° and 0° (latter according to Ref.[137]), $\Delta\theta$ is given as $(\theta_p + \theta_a)/2 = 49°$ and it is assumed $\alpha = 90°$. Fig. 4.13 demonstrates the variation of particle desorption energy in units of $k_BT$. $\gamma_{AO}$ is set to values of 51 and 36mN m$^{-1}$, for water-octane and water-toluene interfaces. The desorption energy of symmetric particles at a WO interface assuming $R_H = 6.4$nm, $\Delta\theta = 0°$, $\alpha = 90°$ is calculated for comparison.
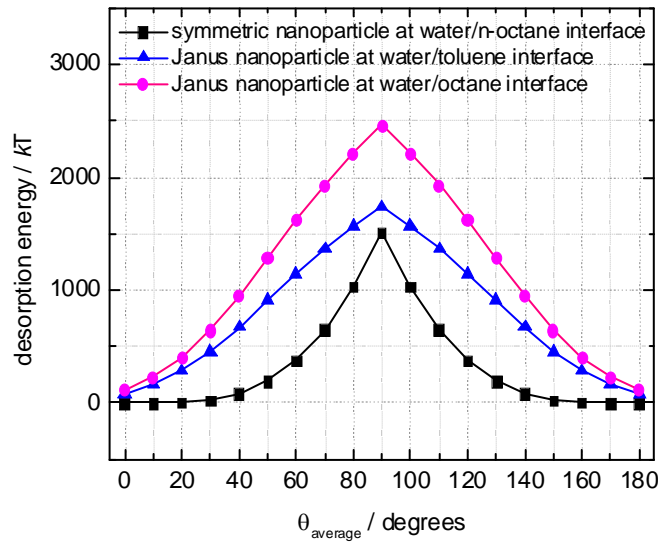
***Figure 4.13***. *Variation of particle desorption energy for symmetric nanopaticles with $R_H$=6.4 nm, $\Delta\theta$ =0°, $\alpha$ =90° at a water/n-octane ($\gamma_{AO}$ = 51mN m$^{-1}$) interface (black squares) and Janus nanopaticles with $R_H$= 5.0nm, $\Delta\theta$ =49°, $\alpha$=90° at water/toluene (blue triangles) and water/n-octane (pink circles) interfaces.*

For Janus nanoparticles at water-tolune and water-octane interfaces, it is interesting to see that the diffusion coefficient is decreased with the increase of the calculated desorption energy. In the past, the desorption energy has been accepted to work on the vertical direction at interfaces. My results present here indicate they may also provide an added force on the diffusing NP in the lateral diffusion. Therefore, further exploration is appealing to find the correlation between the desorption energy and the slowdown of NP diffusion at interfaces.

## 4.3 Discussion

The interfacial behavior of micro-particles and nanoparticles is quite different. Macroscopic theories can notably describe the stability and the interactions of micro-colloids at interfaces [57, 118, 138-140]. Some aspects of the theories may remain valid for NPs, but one could expect new effects e.g. due to stronger influence of thermal fluctuation.

The main finding in this chapter is that the NPs diffuse more slowly when they are at an interface than in the bulk. Our results is in broad agreement with a recent theoretical study [135]. Clearly there is an added force (or friction) on the diffusing nanoparticles in a backward direction parallel to the interfaces. However, as the origin of this added force is not known yet, here I draw some possibilities.

In general, a heterogeneous surface of the particle leads to a zig-zaged three-phase contact line and thus the interface around the particle. In equilibrium this changed interfacial structure is radial symmetric. This symmetry is broken if the particle moves. When a particle diffuses laterally new interfacial area is created behind it while interfacial area is consumed ahead of it. The gain in energy from the disintegration of interface in front can to a large degree not be used to create a new interface behind the particle. Therefore, energy is dissipated. The energy dissipation acts like a local decrease in temperature and diffusion is slowed down.

In addition, there are several factors that are usually omitted in traditional theories. For example, NPs are usually treated as rigid objects and the WO interface is considered as an absolute plane. However, NPs are usually functionalized with flexible organic shells which allow NPs to deform from an idealized spherical shape at interfaces [141]. Then the NP size at interfaces may be deviated from the values which one obtained in the bulk. Moreover, the interface creates a potential well (Figs.1.7 and 4.13) which confines NPs out of the interfacial region. But NPs may oscillate at the vertical direction around the equilibrium position owing to the thermal energy. Energy is required to push nanoparticles back to the equilibrium position. The energy loss acts like the friction coefficient and diffusion is slowed down. The oscillation is expected to occur on the length scale of the WO interface, i.e., roughly 10 angstroms as described by the capillary wave theory [28, 29]. Therefore, only 2D diffusion can be probed by FCS.

As a concluding remark, in this chapter I studied interfacial diffusion of NPs at WO interfaces using FCS. I found that in all cases the interfacial diffusion is slower than that predicted by Stokes-Einstein equation. The slowdown depends on the particle sizes, the

chemical feature on NP surfaces, the interfacial tension and the viscosities of both liquid phases. While the exact mechanism of this slowdown is under investigation, the effect should be considered in all studies and applications for which the dynamics on liquid interfaces is relevant.

# CHAPTER 5

## Summary and Conclusion

In this thesis, I used fluorescence correlation spectroscopy (FCS) to study the diffusion of various fluorescent species at water-oil interfaces. Fluorescence correlation spectroscopy is a prominent technique to monitor the diffusing species coming in and out of a very small observation volume (smaller than $1\mu m^3$) "one at a time". Compared to other techniques, FCS can address the diffusion phenomena at an extremely low concentration, usually down to nanomolar concentration. Most notably, FCS also provides a possibility to access a desired position in a sample locally in which a high spatial resolution is required.

First, I reported a new strategy to study the controversial question of the properties of water/oil interfaces in an angstrom scale. Rather than measuring structural and spectroscopic properties I studied the interfacial properties by monitoring the diffusion coefficient of single molecular tracers as a function of viscosity of both liquid phases and the tracer's size. My results indicated the existence of an interfacial region with a reduced effective viscosity that decayed over a length scale on the order of radius of Rhodamine 6G molecules. I believe that my results have made a strong step forward towards entirely resolving this fascinating question.

Afterwards, I used FCS to measure the interfacial diffusion coefficient of hydrophilic and hydrophobic quantum dots with sizes in the range of 10 - 20 nm adsorbed at water-alkane interfaces. I found that in all cases the interfacial diffusion coefficient depends on the particle size and the viscosity of both liquid phases. Remarkably, compared to the interfacial diffusion

of molecular tracers, the situation is strikingly different for nanoparticles. The interfacial diffusion is slower when they are at the interface rather than in the bulk. My results were in agreement with a recent theoretical study. In addition, the interfacial diffusion of Janus NPs was even slower than that of their symmetric counterparts.

In brief, I have performed a three-year research to explore the dynamic of single fluorescent species, including molecular tracers and NPs at water-oil interfaces using FCS. FCS is a promising technique to study the mobility of objects with a combination of high spatial resolution and high precision. In addition, FCS has an advantage of addressing the situation at an extremely low concentration (usually 1 nM) since the enrichment of surface-active species could disrupt the intrinsic properties of water-oil interfaces. My results showed that the interfacial diffusion was deviated from what Stokes-Einstein equation predicted. The results presented here raised fundamental questions regarding what happened when surface-active species were absorbed at interfaces. It is my hope that these experimental results can call renewed experimental and theoretical attention to resolve the underlying mechanism of diffusion at interfaces.

# Acknowledgments

I would like to thank lots of people who made this thesis possible.

First of all I wish to express my sincere gratitude to Prof. Dr. Hans-Jürgen Butt, for offering me such a good opportunity to study in his Group, and for providing fruitful discussions concerning my work.

My great thanks are given to Dr. Kaloian Koynov, my project leader, who guided me into this exciting research field, directed this work with constantly insightful advice, and help me to figure out the problems I met and also corrected the papers I wrote. I know he had really bad time when he corrected my writing. I really enjoyed working with him.

My thanks go to Prof. Christopher Y. Li for making the interfacial study possible, for offering the precious Janus NPs and for fruitful discussions.

I also would like to express my gratitude to Andrease Best for the technical support with the confocal microscopy and other experimental setups during the time I worked at MPIP.

I like to thank Prof. Ashis Mukhopadhyay who kindly shared all his experience and knowledge about the interfacial study with me.

I should not forget to thank my colleagues, Stoyan Yordanov who always offered me lots of pretty pictures, Dr. Jingfa Yang, Apostolos Vagias, Mikheil Doroshenko for the nice time we spent together. This is really the precious memory.

Finally I want to thank my parents and my wife, for the understanding and support.

# List of symbols

| | |
|---|---|
| c | concentration |
| D | Diffusion coefficient |
| $D_{\parallel}$ | Interfacial diffusion coefficient |
| $D_{bulk}$ | Diffusion coefficient in bulk |
| F(t) | Fluorescence intensity (kHz) at time t |
| G(t) | Autocorrelation function |
| $\lambda$ | Wavelength of light |
| $R_H$ | Hydrodynamic radius |
| N | Number of fluorescence species in the detecting volume |
| $r_0$ | Radial axis of confocal volume |
| $z_0$ | Vertical axis of confocal volume |
| S | Structure of parameter = $z_0/r_0$ |
| t | Experimental lag time |
| $\tau_D$ | Lateral diffusion time |
| T | Temperature |
| V | observation volume |
| $\eta$ | Viscosity |
| $\eta_a$ | Viscosity of alkanes´ phase |
| $\eta_w$ | Viscosity of aqueous´ phase |
| L | Liter |
| M | mol/L |
| n | refractive index |
| s | Seconds |

# List of abbreviations

2D             Two-dimension

3D             Three-dimension

BOC            Butyloxycarbonyl

CTAB           Cetyl trimethylammonium bromide

DLS            Dynamic light scattering

FCS            Fluorescence correlation sspectroscopy

GPC            Gel permeation chromatography

LP             Long pass transmission filter

NP             Nanoparticle

PAEMA          Poly(aminoethyl methacrylate)

PEG            Polyethylene glycol

QD             Quantum dot

$QD_{o-5}$       Organic QD with the $R_H$ of 5nm

$QD_{w-j}$       Water soluble QD with the $R_H$ of j

Rh6G           Rhodamine 6G

SDS            Sodium dodecyl sulfate

WO             Water-oil

# Bibliography

[1]      D. Chandler, Nature **437**, 640 (2005).

[2]      S. Granick, and S. C. Bae, Science **322**, 1477 (2008).

[3]      S. Sastry, Nature **409**, 300 (2001).

[4]      Q. Du, E. Freysz, and Y. R. Shen, Science **264**, 826 (1994).

[5]      L. F. Scatena, M. G. Brown, and G. L. Richmond, Science **292**, 908 (2001).

[6]      M. Sovago *et al.*, Phys. Rev. Lett. **100**, 173901 (2008).

[7]      G. Hura *et al.*, J. Chem. Phys. **113**, 9140 (2000).

[8]      A. Narten, J. Chem. Phys. **56**, 5681 (1972).

[9]      A. K. Soper, and M. A. Ricci, Phys. Rev. Lett. **84**, 2881 (2000).

[10]     L. Bosio, J. Teixeira, and H. E. Stanley, Phys. Rev. Lett. **46**, 597 (1981).

[11]     L. Bosio, J. Teixeira, and M. C. Bellissentfunel, Phys. Rev. A **39**, 6612 (1989).

[12]     V. F. Petrenko, and R. W. Whitworth, *Physics of ice* (Oxford University Press, USA, 1999).

[13]     H. J. Butt *et al.*, *Physics and chemistry of interfaces* (Wiley Online Library, 2003), Vol. 1.

[14]     F. Brochard-Wyart *et al.*, Langmuir **7**, 335 (1991).

[15]     B. Pethica, J. Colloid Interface Sci. **62**, 567 (1977).

[16]     T. Pompe, and S. Herminghaus, Phys. Rev. Lett. **85**, 1930 (2000).

[17]     D. L. Cheung, and S. A. F. Bon, Phys. Rev. Lett. **102,** 066103 (2009).

[18]     F. H. Stillinger, J. Solut. Chem. **2**, 141 (1973).

[19]     K. Lum, D. Chandler, and J. D. Weeks, J. Phys. Chem. B **103**, 4570 (1999).

[20]     C. Sendner *et al.*, Langmuir **25**, 10768 (2009).

[21]     F. Bresme *et al.*, Phys. Rev. Lett. **101,** 056102 (2008).

[22]     J. Mittal, and G. Hummer, Proc. Natl. Acad. Sci. USA **105**, 20130 (2008).

[23]     A. R. Vanbuuren, S. J. Marrink, and H. J. C. Berendsen, J. Phys. Chem. **97**, 9206 (1993).

[24]     Z. Yuhong *et al.*, J. Chem. Phys. **103**, 10252 (1995).

[25]     D. M. Huang, and D. Chandler, J. Phys. Chem. B **106**, 2047 (2002).

[26]     H. S. Ashbaugh, and M. E. Paulaitis, J. Am. Chem. Soc. **123**, 10721 (2001).

[27]     R. Vácha *et al.*, Phys. Chem. Chem. Phys. **10**, 4975 (2008).

[28]     D. M. Mitrinovic *et al.*, Phys. Rev. Lett. **85**, 582 (2000).

[29] K. Kashimoto *et al.*, Phys. Rev. Lett. **101,** 076102 (2008).

[30] L. B. R. Castro, A. T. Almeida, and D. F. S. Petri, Langmuir **20**, 7610 (2004).

[31] M. Mao *et al.*, Langmuir **20**, 1843 (2004).

[32] Y. Takata *et al.*, Langmuir **22**, 1715 (2006).

[33] J. P. R. Day, and C. D. Bain, Phys. Rev. E **76** (2007).

[34] Y. S. Seo, and S. Satija, Langmuir **22**, 7113 (2006).

[35] D. A. Doshi *et al.*, Proc. Natl. Acad. Sci. USA **102**, 9458 (2005).

[36] M. Maccarini *et al.*, Langmuir **23**, 598 (2006).

[37] R. Steitz *et al.*, Langmuir **19**, 2409 (2003).

[38] D. Schwendel *et al.*, Langmuir **19**, 2284 (2003).

[39] S. M. Dammer, and D. Lohse, Phys. Rev. Lett. **96,** 206101 (2006).

[40] D. Bratko, and A. Luzar, Langmuir **24**, 1247 (2008).

[41] M. Mezger *et al.*, Proc. Natl. Acad. Sci. USA **103**, 18401 (2006).

[42] A. Poynor *et al.*, Phys. Rev. Lett. **97,** 266101 (2006).

[43] T. R. Jensen *et al.*, Phys. Rev. Lett. **90**, 4 (2003).

[44] B. M. Ocko, A. Dhinojwala, and J. Daillant, Phys. Rev. Lett. **101,** 039601 (2008).

[45] M. Mezger *et al.*, J. Chem. Phys. **128**, 244705 (2008).

[46] M. Mezger *et al.*, J. Am. Chem. Soc. **132**, 6735 (2010).

[47] S. Chattopadhyay *et al.*, Phys. Rev. Lett. **105,** 037803 (2010).

[48] M. Mezger *et al.*, Phys. Rev. Lett. **107**, 249801 (2011).

[49] S. U. Pickering, J. Chem. Soc. Trans **91**, 2001 (1907).

[50] Y. Lin *et al.*, Science **299**, 226 (2003).

[51] H. W. Duan *et al.*, Angew. Chem., Int. Ed. **43**, 5639 (2004).

[52] F. Bresme, and M. Oettel, J. Phys.-Condes. Matter **19,** 413101 (2007).

[53] P. Arumugam *et al.*, J. Am. Chem. Soc. **130**, 10046 (2008).

[54] B. P. Binks, and S. O. Lumsdon, Langmuir **17**, 4540 (2001).

[55] B. P. Binks, and J. A. Rodrigues, Angew. Chem., Int. Ed. **44**, 441 (2005).

[56] B. P. Binks, and J. A. Rodrigues, Angew. Chem., Int. Ed. **46**, 5389 (2007).

[57] P. Pieranski, Phys. Rev. Lett. **45**, 569 (1980).

[58] B. P. Binks, and S. O. Lumsdon, Langmuir **16**, 8622 (2000).

[59] R. Aveyard, and J. H. Clint, J. Chem. Soc.-Faraday Trans. **92**, 85 (1996).

[60] H. Fan, D. E. Resasco, and A. Striolo, Langmuir **27**, 5264 (2011).

[61] D. L. Cheung, J. Chem. Phys. **135**, 054704 (2011).

[62] D. L. Cheung, and S. A. F. Bon, Soft Matter **5**, 3969 (2009).

[63] F. Reincke *et al.*, Phys. Chem. Chem. Phys. **8**, 3828 (2006).

[64]    K. Larson-Smith, A. J. Jackson, and D. C. Pozzo, Langmuir **28,** 2493 (2012).

[65]    A. Boeker *et al.*, Soft Matter **3**, 1231 (2007).

[66]    N. Glaser *et al.*, Langmuir **22**, 5227 (2006).

[67]    B. P. Binks, and P. D. I. Fletcher, Langmuir **17**, 4708 (2001).

[68]    P. Saffman, and M. Delbrück, Proc. Natl. Acad. Sci. **72**, 3111 (1975).

[69]    B. Radoev, M. Nedyalkov, and V. Dyakovich, Langmuir **8**, 2962 (1992).

[70]    H. Brenner, and L. G. Leal, J. Colloid interf. Sci. **65**, 191 (1978).

[71]    T. M. Fischer, P. Dhar, and P. Heinig, J. Fluid Mech. **558**, 451 (2006).

[72]    J. Wu, and L. L. Dai, Langmuir **23**, 4324 (2007).

[73]    Y. Peng *et al.*, J. Fluid Mech. **618**, 243 (2009).

[74]    Y. Song, M. Luo, and L. L. Dai, Langmuir **26**, 5 (2009).

[75]    D. L. Cheung,  Chem. Phys. Lett. **495**, 55 (2010).

[76]    Y. Lin *et al.*, Langmuir **21**, 191 (2005).

[77]    S. Kutuzov *et al.*, Phys. Chem. Chem. Phys. **9**, 6351 (2007).

[78]    A. Stocco *et al.*, Phys. Rev. E **83**, 011601 (2011).

[79]    T. Cherdhirankorn *et al.*, Macromolecules **42**, 9183 (2009).

[80]    T. Cherdhirankorn *et al.*, Macromolecules **42**, 4858 (2009).

[81]    J. Zhao, and S. Granick, J. Am. Chem. Soc. **126**, 6242 (2004).

[82]    J. F. Yang, J. Zhao, and C. C. Han, Macromolecules **41**, 7284 (2008).

[83]    S. Ramadurai *et al.*, J. Am. Chem. Soc. **131**, 12650 (2009).

[84]    J. S. S. Wong *et al.*, Macromolecules **44**, 3073 (2011).

[85]    D. Magde, E. Elson, and W. Webb, Phys. Rev. Lett. **29**, 705 (1972).

[86]    D. Magde, E. L. Elson, and W. W. Webb, Biopolymers **13**, 29 (1974).

[87]    R. Rigler *et al.*, Euro. Biophys. J. **22**, 169 (1993).

[88]    E. Haustein and P. Schwille, Annu. Rev. Biophys. Biomol. Struct. **36,** 151 (2007)

[89]    A. Goebel, and K. Lunkenheimer, Langmuir **13**, 369 (1997).

[90]    S. Zeppieri, J. Rodriguez, and A. L. L. de Ramos, J. Chem. Eng. Data **46**, 1086 (2001).

[91]    M. Yin *et al.*, J. Am. Chem. Soc. **130**, 7806 (2008).

[92]    C. Kohl *et al.*, Chem.-Eur. J. **10**, 5297 (2004).

[93]    B. Li, and C. Y. Li, J. Am. Chem. Soc. **129**, 12 (2007).

[94]    B. Wang *et al.*, J. Am. Chem. Soc. **130**, 11594 (2008).

[95]    R. Rigler, and E. Elson, *Fluorescence correlation spectroscopy: theory and applications* (Springer Verlag, 2001).

[96]    J. Donsmark, and C. Rischel, Langmuir **23**, 6614 (2007).

[97]    C. B. Mueller *et al.*, EPL **83**, 46001 (2008).

[98]    M. Eigen, and R. Rigler, Proc. Natl. Acad. Sci. USA **91**, 5740 (1994).

[99]    M. Negishi *et al.*, Langmuir **24**, 8431 (2008).

[100]   J. A. McGuire, and Y. R. Shen, Science **313**, 1945 (2006).

[101]   C. S. Hsieh *et al.*, Phys. Rev. Lett. **107**, 116102 (2011).

[102]   Z. Zhang *et al.*, Nature Chem **3**, 888 (2011).

[103]   M. Smits *et al.*, Phys. Rev. Lett. **98**, 98302 (2007).

[104]   L. Bosio, J. Teixeira, and H. E. Stanley, Phys. Rev. Lett. **46**, 597 (1981).

[105]   Y. Xie *et al.*, Phys. Rev. Lett. **71**, 2050 (1993).

[106]   O. Magnussen *et al.*, Phys. Rev. Lett. **74**, 4444 (1995).

[107]   D. S. Walker, and G. L. Richmond, J. Am. Chem. Soc. **129**, 9446 (2007).

[108]   M. Mezger *et al.*, Science **322**, 424 (2008).

[109]   M. K. Sanyal *et al.*, Phys. Rev. Lett. **66**, 628 (1991).

[110]   J. M. Kovaleski, and M. J. Wirth, J. Phys. Chem. **99**, 4091 (1995).

[111]   D. Wang *et al.*, Small **7**, 3502 (2011).

[112]   K. Masschaele *et al.*, Phys. Rev. Lett. **105,** 048303(2010).

[113]   Y. J. Li, W. I. J. Huang, and S. G. Sun, Angew. Chem., Int. Ed. **45**, 2537 (2006).

[114]   B. Samanta *et al.*, Angew. Chem., Int. Ed. **48**, 5341 (2009).

[115]   M. E. Flatte, A. A. Kornyshev, and M. Urbakh, J. Phys.-Condes. Matter **20,** 073102 (2008).

[116]   L. Isa *et al.*, Nat. Commun. **2**, 438 (2011).

[117]   B. D. Hughes, B. A. Pailthorpe, and L. R. White, J. Fluid Mech. **110**, 349 (1981).

[118]   R. Aveyard *et al.*, Phys. Rev. Lett. **88,** 246102 (2002).

[119]   T. S. Horozov *et al.*, Langmuir **21**, 7405 (2005).

[120]   D. Frydel, S. Dietrich, and M. Oettel, Phys. Rev. Lett. **99,** 118302 (2007).

[121]   B. J. Park, and E. M. Furst, Soft Matter **7**, 7676 (2011).

[122]   S. Jiang *et al.*, Adv. Mater. **22**, 1060 (2010).

[123]   B. Wang *et al.*, J. Am. Chem. Soc. **130**, 11594 (2008).

[124]   B. Dong, B. Li, and C. Y. Li,  J. Mater. Chem. **21**, 13155 (2011).

[125]   L. Isa *et al.*, CHIMIA **64**, 145 (2010).

[126]   L. Isa *et al.*, Soft Matter **7**, 7663 (2011).

[127]   B. J. Park, T. Brugarolas, and D. Lee, Soft Matter **7**, 6413 (2011).

[128]   L. Hong *et al.*, Langmuir **24**, 621 (2008).

[129]   Q. Chen *et al.*, Science **331**, 199 (2011).

[130]   B. J. Park, J. Vermant, and E. M. Furst, Soft Matter **6**, 5327 (2010).

[131]   T. Bickel, Phys Rev E **75,** 041403 (2007).

[132]   G. M. Wang, R. Prabhakar, and E. M. Sevick, Phys. Rev. Lett. **103,** 248303 (2009).

[133]   D. Abras, G. Pranami, and N. L. Abbott, Soft Matter **8**, 2026 (2012).

[134]   K. Du, J. A. Liddle, and A. J. Berglund, Langmuir **28**, 9181 (2012).

[135]   J. Bławzdziewicz, M. Ekiel-Jeżewska, and E. Wajnryb, J. Chem. Phys. **133**, 114702 (2010).

[136]   B. J. Park, and D. Lee, ACS Nano **6**, 782 (2012).

[137]   S. Jiang, and S. Granick, J. Chem. Phys. **127,** 161102 (2007).

[138]   A. Scheludko, B. V. Toshev, and D. T. Bojadjiev, J. Chem. Soc.-Faraday Trans. **72**, 2815 (1976).

[139]   V. N. Paunov *et al.*, J. Colloid Interface Sci. **157**, 100 (1993).

[140]   B. P. Binks, Curr. Opin. Colloid Interface Sci. **7**, 21 (2002).

[141]   R. Ranatunga *et al.*, J. Phys. Chem. C **114**, 12151 (2010).
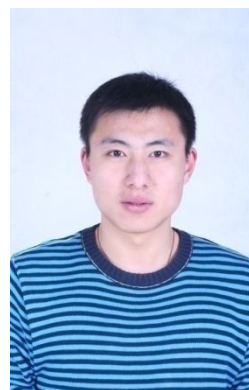
# List of publications

1. <u>Wang D, et al.</u> Small. 7(24), 3502-3507 (2011)


2. Chen J, <u>Wang D</u>, et al. Polymer Chemistry (accepted).


3. Nguyen T, Türp D, <u>Wang D</u>, et al. Journal of the American Chemical Society 2011;133(29):11194-11204.

# Curriculum Vitae

**Personal Information**

| | | |
|---|---|---|
| **Name** | WANG Dapeng | |
| **Address** | Ackermannweg 10 | |
| | 55128, Mainz | |
| | Germany | |
| **Citizenship** | Chinese | |

**Education**

Sept. 2009- present   **Max Planck Institute for Polymer Research**

PhD student of Physical Chemistry

Degree to be obtained: Doctor in natural science (Dr. rer. nat)

Sept. 2006- Jul.2009  **Qingdao University of Science & Technology (China)**

Master of Science, in Polymer Chemistry & Physics

Sept. 2002- Jul.2006  **Qingdao University of Science & Technology (China)**

Bachelor of Engineering, in Polymer Materials & Engineering

**Publications**

1. <u>D. P. Wang</u>, S. Yordanov, H. M. Paroor, A. Mukhopadhyay, C. Y. Li, H.-J. Butt, K. Koynov. Probing Diffusion of Single Nanoparticles at Water-Oil Interfaces. Small. 7(24), 3502-3507 (2011)

**Presentations**

1. 25th European Colloid and Interface Society Conference, Germany, 2011

   Dapeng Wang, Kaloian Koynov, Hans-Jürgen Butt, Probing Diffusion of Single Nanoparticles at Water-oil Interfaces with Fluorescence Correlation Spectroscopy. (poster)

2. 8th Zsigmondy Colloquium of the German Colloid Society , Germany, 2012

   Dapeng Wang, Kaloian Koynov, Hans-Jürgen Butt, Probing Diffusion of Single Nanoparticles at Water-oil Interfaces with Fluorescence Correlation Spectroscopy. (poster)